Structural basis for regulation of a tripartite toxin-antitoxin system by dual phosphorylation

René L. Bærentsen[1], Stine Vang Nielsen[2*], Jeppe Lyngsø[3], Francesco Bisiak[1], Jan Skov Pedersen[3], Kenn Gerdes[4], Michael A. Sørensen[2†], Ditlev. E. Brodersen[1†]*

[1]Department of Molecular Biology and Genetics, Aarhus University, Gustav Wieds Vej 10c, DK-8000 Aarhus C, Denmark, [2]Department of Biology, University of Copenhagen, Ole Maaløes Vej 5, DK-2200 København N, [3]Department of Chemistry and Interdisciplinary Nanoscience Centre (iNANO), Gustav Wieds Vej 14, DK-8000 Aarhus C, [4]Voldmestergade 8, DK-2100 København Ø, Denmark.

[*]These authors contributed equally.

[†]To whom correspondence should be addressed (mas@bio.ku.dk, phone +45 35323711 or deb@mbg.au.dk, phone +45 21669001).

Keywords: HipBA; STK; Ser/Thr kinase; TrpS; tRNA synthetase

Running title: Regulation of a tripartite TA system

ABSTRACT

Many bacteria encode multiple toxin-antitoxin (TA) systems targeting separate, but closely related, cellular functions. The toxin of the *E. coli hipBA* system, HipA, is a kinase that inhibits inhibits translation via phosphorylation of glutamyl-tRNA synthetase. Enteropathogenic *E. coli* (EPEC) O127:H6 encodes an additional, tripartite TA module, *hipBST*, for which the HipT toxin was shown to specifically target tryptophanyl-tRNA synthetase, TrpS. Surprisingly, the function as antitoxin has been taken over by the third protein, HipS, but the molecular details of how activity of HipT is controlled remain poorly understood. Here, we show that HipBST is markedly different from HipBA and that the unique HipS protein, which is homologous to the N-terminal subdomain of HipA, has evolved to function as antitoxin by breaking the kinase active site. We also show how auto-phosphorylation at two conserved sites in the kinase toxin serve to dually regulate binding of HipS and kinase activity. Finally, we demonstrate that the HipBST complex is dynamic and present a cohesive model for the regulation and activation of this type of three-component system.

15 **INTRODUCTION**

16 Bacteria employ a wide range of mechanisms adapt to changing environments and imminent threats
17 such as antibiotics and phage attack, including activation of toxin-antitoxin (TA) systems that can
18 release intracellular toxins to rapidly alter metabolism or reduce growth (Harms et al., 2018).
19 Canonical (type II) TA systems are small, bicistronic loci that encode a protein toxin and its cognate
20 antidote (antitoxin) that tightly interact to form a higher-order complex in the inactive state, usually
21 capable of controlling transcription via a DNA-binding domain on the antitoxin (Harms et al., 2018).
22 There are also examples of tricistronic TA loci, in which the third component is either a chaperone
23 required for folding of the antitoxin and thus, toxin inhibition (Bordes et al., 2016) or an additional,
24 transcriptional regulator (Hallez et al., 2010; Zielenkiewicz & Ceglowski, 2005). A striking
25 observation is that some microorganisms contain a very large number of similar, paralogous TA
26 systems, such as the human pathogen, *Mycobacterium tuberculosis*, which contains at least 47
27 paralogous TA systems of the *vapBC*-type, for which the VapC toxin appears to target unique non-
28 coding RNA species (Sharrock et al., 2018; Winther et al., 2016). Likewise, *Salmonella enterica*
29 encodes several paralogous *tacTA* systems in which the TacT toxins function by acetylating the
30 primary amine of amino acids of charged transfer RNA molecules (Grabe et al., 2021). These cases
31 raise important questions about the evolutionary benefit of harbouring multiple, highly similar toxin
32 systems as well as how cross-reactivity is prevented.

33

34 In the widespread and diverse *hipBA* (high persister) system, the HipA toxin is a serine-threonine
35 kinase (STKs) (Hanks et al., 1988; Stancik et al., 2018), while the cognate antitoxin, HipB, contains
36 a helix-turn-helix (HTH) motif and inhibits the toxin by a mechanism which is not fully understood
37 (Gerdes et al., 2021; Schumacher et al., 2009). In the most well-studied and canonical *hipBA* system
38 in *Escherichia coli* K-12, the toxin ($HipA_{Ec}$) specifically targets glutamyl-tRNA synthetase (GltX)

39 by phosphorylation of an ATP-binding motif conserved in type I aminoacyl-tRNA synthetases (Eriani
40 et al., 1990; Sekine et al., 2003), thereby inhibiting its activity and blocking translation (Germain et
41 al., 2013). Accumulation of uncharged $tRNA^{Glt}$ subsequently induces the stringent response via RelA-
42 mediated (p)ppGpp synthesis on starved ribosomes (Haseltine & Block, 1973; Pacios et al., 2020;
43 Winther et al., 2018). In contrast to most type II TA systems, the cognate antitoxin, HipB does not
44 directly interact with the HipA active site and inhibition has therefore been proposed to occur by
45 several mechanisms, including blocking conformational changes in the kinase required for catalysis,
46 sequestration of HipA on DNA via the HipB DNA binding domain (Schumacher et al., 2009), or
47 allosterically via placement of a C-terminal Trp residue of HipB into a pocket on HipA (Evdokimov
48 et al., 2009). In an additional layer of complexity in regulation, $HipA_{Ec}$ is regulated by *trans*
49 autophosphorylation at a conserved serine (Ser150) situated in a loop (the "Gly-rich loop") near the
50 active site, which is required for ATP binding and functionally similar to the P loop in eukaryotic
51 kinases (Huse & Kuriyan, 2002; Schumacher et al., 2012). Phosphorylation at this site causes a
52 conformational change in which the loop is ejected from its burrowed position inside the active site,
53 rendering the kinase unable to bind ATP (Schumacher et al., 2012).
54
55 Enteropathogenic *E. coli* (EPEC) O127:H6, an important diarrheal pathogen of young children,
56 contains, in addition to the canonical *hipBA* locus, a homologous tricistronic TA system, *hipBST*,
57 encoding three separate proteins. HipB, by analogy to HipBA, contains a putative DNA-binding HTH
58 domain while HipT is a kinase like HipA and functions as toxin by phosphorylating and inactivating
59 tryptophanyl-tRNA, TrpS (Gerdes et al., 2021; Vang Nielsen et al., 2019). Surprisingly, the third
60 protein, HipS, which at the sequence level corresponds to the N-terminal subdomain 1 of the larger
61 HipA kinase, was shown to function as antitoxin by an unknown mechanism (Vang Nielsen et al.,
62 2019). Moreover, HipT was shown to be subject to autophosphorylation at two conserved serine

63 positions in the Gly-rich loop, but the functional consequences of this are also not known. Here, we
64 show that the HipBST complex fom pathogenic *E. coli* is markedly different from HipBA and that
65 inhibition of HipT is achieved through direct interaction with a conserved residue in HipS. Two
66 structures of HipT in separate, phosphorylated states further demonstrate that HipT, is found in an
67 inactive conformation regardless of phosphorylation state inside the HipBST complex. Finally, we
68 show, using phosphomimetic kinase variants *in vivo* and analysis of phosphorylation patterns and
69 flexibility *in vitro*, that the two phosphorylation positions control HipT activity and binding of
70 antitoxin (HipS), and that the HipBST complex is dynamic. Together, our data provide a mechanistic
71 understanding of how the HipS protein can function as antitoxin and suggests that the corresponding
72 domain in HipA can have important, regulatory roles as well.
73
74 **RESULTS**
75 **Dual autophosphorylation sites are conserved in HipT kinases**
76 One of the most surprising features of the HipBST system is that HipS shows sequence similarity to
77 the N-terminal subdomain 1 of HipA, the toxin of the *hipBA* system, while simultaneously
78 functioning as antitoxin (**Figure S1**) (Vang Nielsen et al., 2019). Moreover, phylogenetic analysis
79 has demonstrated that HipT and HipA toxins are relatively closely related within a very broad
80 superfamily of HipA-homologous kinases (Gerdes et al., 2021). To gain further insight into the basis
81 of this important difference, we initially performed a focused phylogenetic analysis of the 48 HipT
82 orthologues identified so far among bacterial genomes (Gerdes et al., 2021). Alignment and clustering
83 reveals a largely bifurcated, phylogenetic tree for which one large branch (the "SIS group") contains
84 HipT kinases with two serine residues in close proximity in the Gly-rich loop corresponding to the
85 known autophosphorylation sites in HipT of *E. coli* O127:H6 (**Figure 1a**). In the remainder of the
86 HipT orthologues, this region contains variable Ser/Thr motifs, including TxT, Sxx, xxT, SxT, and
87

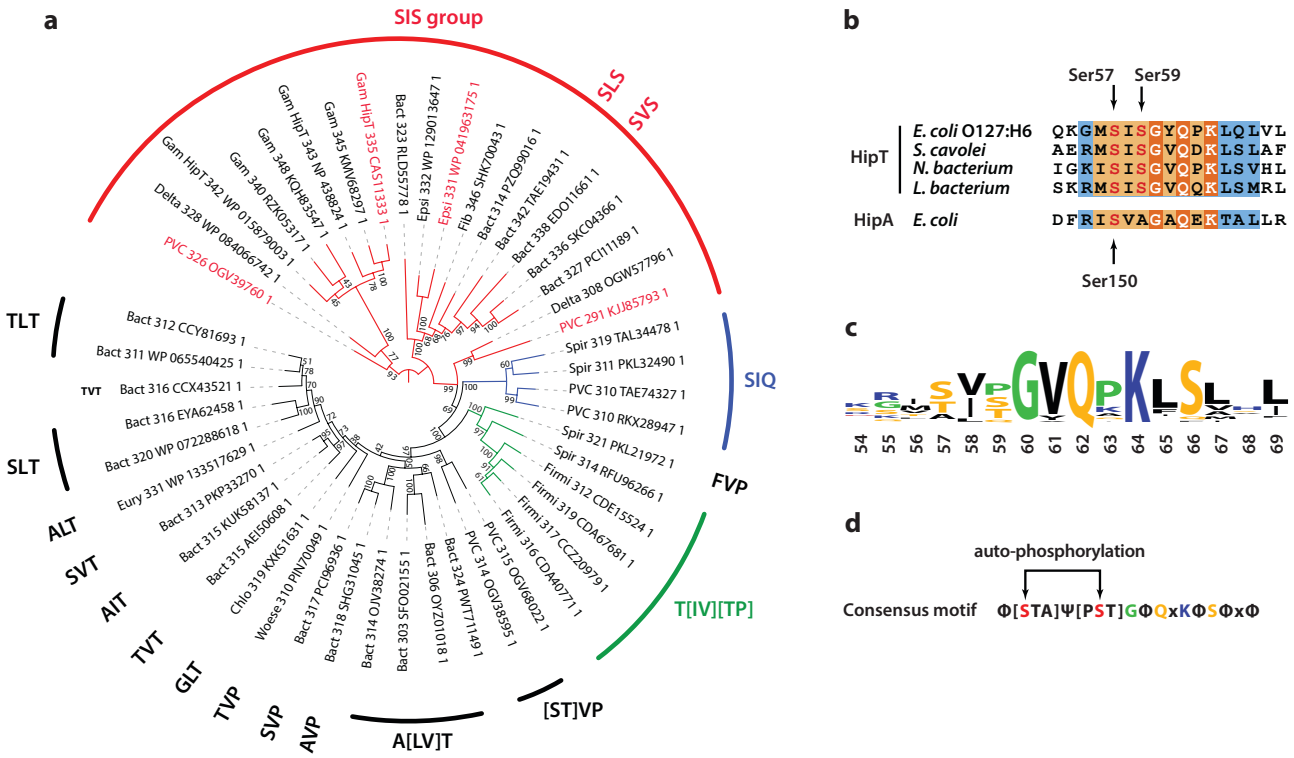

Figure 1. Phylogenetic analysis of HipT. a. Phylogenetic guide tree of 48 HipT orthologues with sequences motifs (potential phosphorylation sites) indicated on the side. The "SIS group" (red) is by far the largest group followed by the T[IV][TP] group (green), and SIQ group (blue). Sequences used in the alignment in **b** are shown with red letters. Numbers on the branches indicate bootstrap confidence levels. **b.** Sequences of the Gly-rich loop (orange background), including the potential phosphorylation sites for selected HipT orthologues compared to HipA from *E. coli* K-12. Known phosphorylation sites in *E. coli* O127:H6 HipT (top) and *E. coli* K-12 HipA (bottom) are indicated with arrows and conserved sequence motifs with bold white text. **c.** Sequence logo for the Gly-rich loop derived from all 48 HipT sequences. **d.** Consensus motif for the HipT Gly-rich loop with known phosphorylation sites in red. Φ indicates a hydrophobic residue, while Ψ are aliphatic residues.

99 Txx. We note that the single position between the two Ser/Thr residues invariably is occupied by a
100 small hydrophobic residue (I, L, or V) and that a small subbranch close to the SIS group represents
101 an interesting variation with a Gln in the second autophosphorylation position (the "SIQ" group). The
102 remainder of the Gly-rich loop across a range of HipT kinases is highly similar to $HipA_{Ec}$, which has
103 the sequence ISVAGAQEK (**Figure 1b-c**). We can thus derive a consensus motif for the HipT Gly-
104 rich loop, which includes several conserved hydrophobic positions in addition to the two Ser/Thr
105 residues (**Figure 1d**). In summary, phylogenetic analysis reveals that a large fraction of HipT kinases
106 contain a conserved SIS motif with two potential phosphorylation positions in their Gly-rich loops
107 but also that this region displays some sequence diversity, which may point to subtle differences in
108 regulation.
109
110 **HipBST forms a hexameric higher-order complex**
111 Comparison of the HipBST and HipBA sequences reveals that HipS shows similarity to the N-
112 terminal subdomain 1 of HipA (**Figure S1 and S2a**) and that both HipB and HipT of *hipBST* contain
113 N-terminal extensions of around 35 residues not found in HipB and HipA of *hipBA*, respectively
114 (**Figure 2a and S1**). To understand the molecular basis for the functional and structural differences,
115 we determined the crystal structure of HipBST from enteropathogenic *E. coli* O127:H6 expressed
116 with inactive HipT (D233Q) to 2.9 Å by molecular replacement using $HipA_{Ec}$ as search model
117 (**Figure 2b**). The refined structure (R=19.5% / R_{free}=22.8%) has two copies of each of the three
118 proteins in the asymmetric unit and is generally well-defined for HipB and HipT, while HipS appears
119 to be more flexible. Analysis by the protein interaction server, PISA (Krissinel & Henrick, 2007),
120 suggests that the biological assembly is comprised of a dimer of HipBST heterotrimers, which are
121 held together through dimerisation of HipB (**Figure 2b**). This is consistent with the observation that
122 the HTH domain is usually found as a dimer in DNA-binding proteins (Brennan & Matthews, 1989).
123

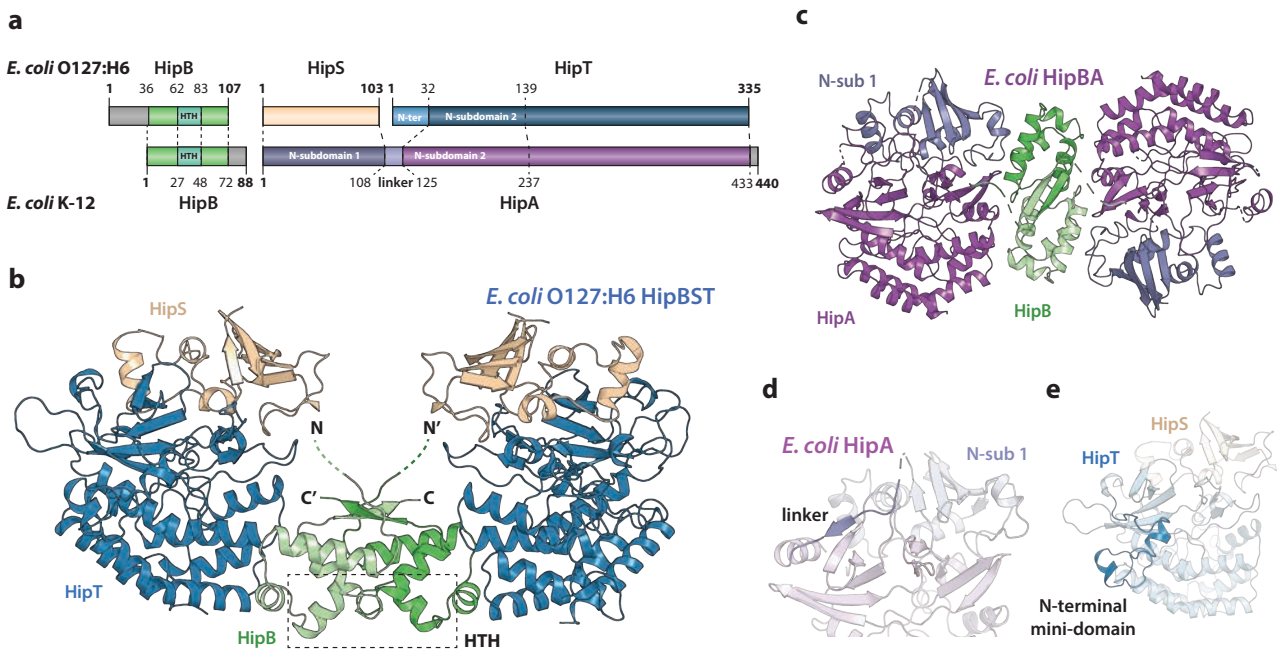

Figure 2. Crystal structure of the *E. coli* O127:H6 HipBST complex. a. Schematic representation of *E. coli* O127:H6 HipBST and canonical *E. coli* HipBA showing corresponding proteins and domains. Dashed lines indicate similar domains and grey areas represent regions missing domains in the crystal structures. HipS (beige) is structurally similar to the N-subdomain 1 of HipA (dark purple), HipT has an additional N-terminal mini-domain not found in HipA (light blue) while HipA has a short linker between the two N-subdomains (light purple). **b.** *E. coli* O127:H6 HipBST forms a hetero-hexameric complex with HipS (beige) on top of HipT (blue) through dimerisation of HipB (green) also generating a helix-turn-helix DNA-binding motif (HTH, dashed box). **c.** Crystal structure of the *E. coli* K-12 HipBA complex (PDB: 2WIU) shown as cartoon with HipA in blue purple (N-terminal subdomain 1) and purple and the HipB homodimer in two shades of green (Evdokimov et al., 2009). **d.** The linker between N-subdomain 1 and 2 (dark purple) physically linking the two domains in $HipA_{Ec}$. **e.** The N-terminal mini-domain of HipT (blue), which is absent from HipA.

138 In this complex, the two HipB monomers interact strongly (interface area = 1,405 $Å^2$) while the
139 interface between HipB and HipT is relatively small (513 $Å^2$). The biological relevance of the hetero-
140 hexamer is supported by analytical gel filtration (**Figure S2b**) and small-angle X-ray scattering
141 (SAXS, **Figure S6**), the latter of which showed a major species with a total mass of 129 $\pm$ 8 kDa, in
142 good agreement with the theoretical mass of 125.6 kDa. HipB consists of an α-helical bundle of four
143 helices including the predicted DNA-binding HTH motif (residues 62-83), which forms a canonical
144 HTH DNA-binding domain exposed at the bottom of the hetero-hexamer (**Figure 2b**). The helical
145 bundle is followed by a small β strand that forms an antiparallel sheet through pairing with the
146 corresponding region in the neighbouring molecule of HipB. The N-terminal extension of HipB (36
147 residues) is not visible in the electron density, but secondary structure prediction indicates that it
148 forms a long α-helix (**Figure S1a**). HipS is closely associated with HipT and consists of a solvent-
149 facing, five-stranded, anti-parallel β sheet of which four strands are located in the N terminus
150 (residues 1-52). These are followed by a small domain of three helices (residues 53-94) that forms
151 the interface to HipT followed by the fifth β strand (residues 95-102, **Figure 2b and S3a**).
152
153 The overall architecture of the HipBST complex consists of two HipST toxin:antitoxin complexes
154 separated in space by the dimer of the HipB and in this way differs markedly different from $HipBA_{Ec}$
155 in which two HipA toxins are closely packed head-to-tail around two HipB antitoxins (**Figure 2c**).
156 This configuration is key to the proposed way in which HipB can function as antitoxin, namely by
157 restricting the movement of the N-terminal subdomain of HipA (**Figure 2c**, blue) (Schumacher et al.,
158 2009). As suggested from sequence analysis, HipS bears a striking structural resemblance to the N-
159 terminal subdomain 1 of HipA (Schumacher et al., 2012), both with respect to its overall fold and
160 placement in relation to HipT. As a result of this, the HipS C-terminus overlaps with a extended linker
161 that bridges N-subdomain 1 to N-subdomain 2 in HipA (**Figure 2d**). HipT corresponds structurally

162 to the core kinase fold of HipA, except for the presence of an additional N-terminal mini-domain
163 (residues 1-41), the role of which is possibly to anchor N-subdomain 2 (residues 42-140) to the core
164 of the kinase in the absence of the physical coupling to HipS **(Figure 2a and 2e)**. Interestingly, the
165 overall structure of the HipBST complex is reminiscent of the structure of a HipBA complex from
166 *Shewanella oneidensis*, which was crystallised in complex with DNA **(Figure S2c)** (Wen et al.,
167 2014). This suggests that the open conformation is not a specific result the tripartite configuration
168 and superpositioning of the DNA-binding domains (**Figure S3b**) and analysis of potential interactions
169 with DNA (**Figure S3c**) suggests HipBST could bind DNA in a similar way.
170
171 **HipT has an inactive conformation inside the HipBST complex**
172 For $HipA_{Ec}$, two discrete active site conformations are observed depending on phosphorylation state
173 and whether substrate (ATP) is bound or not (Schumacher et al., 2015; Schumacher et al., 2012;
174 Schumacher et al., 2009). In its non-phosphorylated form and in the presence of ATP, the flexible
175 Gly-rich loop is found in an inward conformation in which main chain amino groups on Ala154 and
176 Gln155 coordinate the ATP phosphate groups (**Figure 3a**) (Schumacher et al., 2009).
177 Phosphorylation of Ser150, however, causes ejection of the loop through strong interactions of the
178 phosphate group with active sites residues, which prevents binding of ATP (**Figure 3b**) (Schumacher
179 et al., 2012). In the HipBST crystal structures, we find the Gly-rich loop of HipT forms a short α-
180 helix and is in a conformation most similar to the ejected form of the $HipA_{Ec}$ loop despite HipT not
181 being phosphorylated (**Figure 3c**). In this conformation, Ser59, which is known to undergo
182 autophosphorylation in HipT, forms interactions to several active site residues, including Asp210 and
183 the Ser57 auto-phosphorylation site (Vang Nielsen et al., 2019). We conclude that inside the HipBST
184 complex, HipT in its non-phosphorylated state is maintained in an inactive conformation that does
185 not support ATP binding.
186

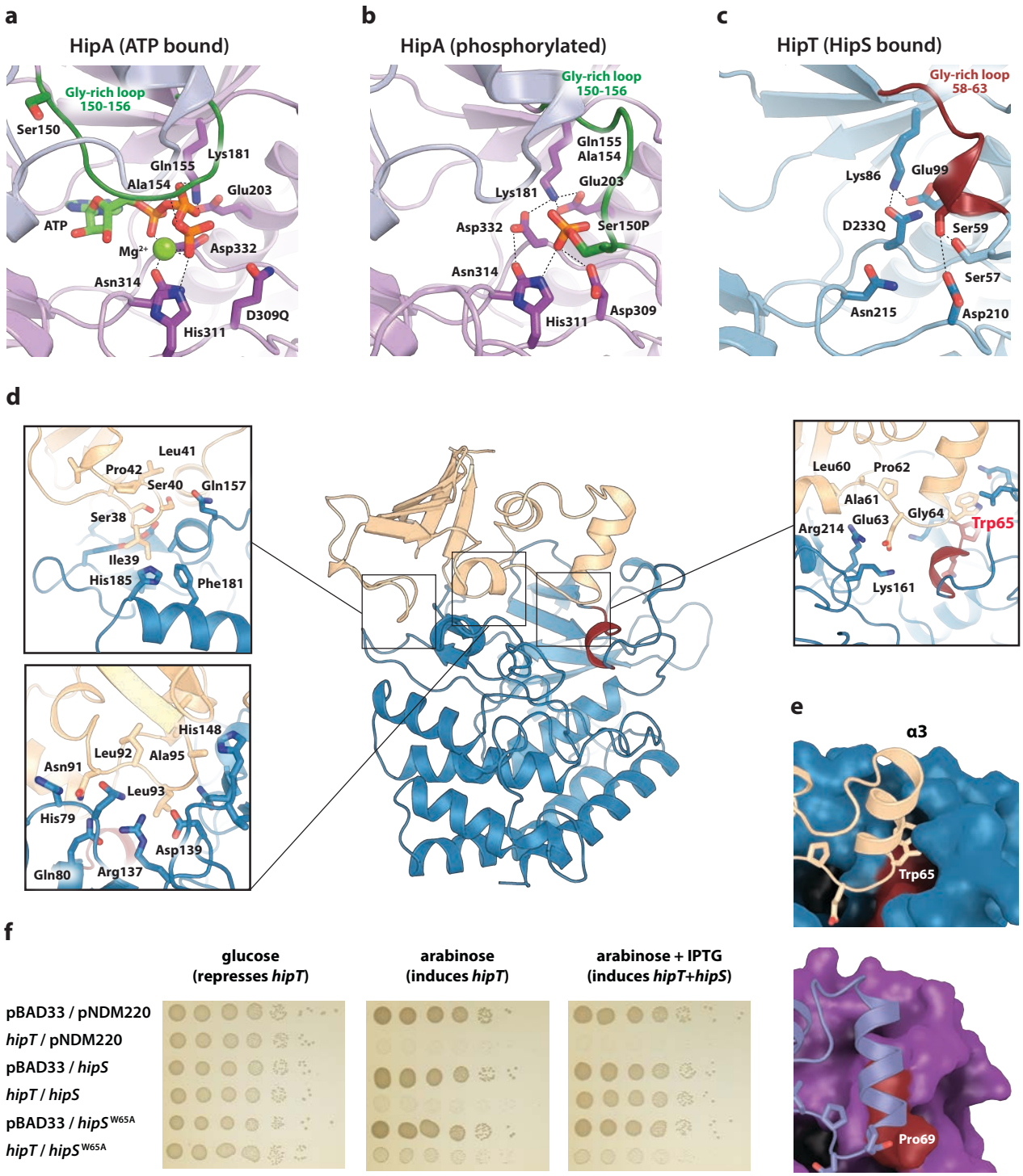

Figure 3. Trp65 is essential for HipS to function as antitoxin. a. Overview of the HipA active site, bound to ATP (green, PDB: 3DNT) (Schumacher et al., 2009). Residues interacting with the nucleotide are highlighted as well as the Gly-rich loop (residues 150-156, green) including Ser150. D309Q is a mutated active site residue. **b.** The active site of HipA phosphorylated on Ser 150 (green/orange, PDB: 3TPE) with the Gly-rich loop (green) in the outward-

192 facing conformation (Schumacher et al., 2012). **c.** The active site of HipBS-bound HipT^{D233Q} with the Gly-rich loop
193 (residues 58-63, ruby) in the outward-facing conformation. D233Q is the mutated active site residue. **d.** Overview
194 and detailed interactions between HipS (beige) and HipT (blue) with its Gly-rich loop (ruby) and interacting residues
195 indicated. **e.** Top, HipS Trp65 (beige) is placed in a pocket on the surface of HipT (blue); Bottom, the corresponding
196 residue (Pro69) in HipA (purple, PDB: 3TPD). **f.** *E. coli* MG1655 harbouring empty pBAD33 vector ("pBAD33")
197 or pSVN1 (pBAD33::*hipT*) in combination with empty pNDM220 vector ("pNDM220"), pSVN109
198 (pNDM220::*hipS*), or pSVN178 (pNDM220::*hipS*^{W65A}) as indicated. Plates contained 0.2% glucose (to repress
199 *hipT*), 0.2% arabinose (to induce *hipT*), or 0.2% arabinose plus 200 μM IPTG (to induce *hipS*, or *hipS*^{W65A}). The
200 plates are representative of at least three independent experiments.
201
202

203 **HipS inhibits HipT through insertion of a hydrophobic residue near the active site**

204 To understand how HipS, which is homologous to the N-terminal subdomain 1 of HipA, can function
205 as the antitoxin in the HipBST system, we then focused on the specific interactions found between
206 HipS and HipT. There are three major areas of contact between the two proteins with several strong
207 interactions on both sides of the kinase domain, involving both hydrogen bonds and hydrophobic and
208 charged interactions (**Figure 3d**). Near the Gly-rich loop, HipS Glu63 points directly into the HipT
209 active site while Trp65 is wedged into a deep cavity formed by the HipT Gly-rich loop in its outward
210 conformation. While Glu63 is conserved in the N-terminal subdomain of $HipA_{Ec}$ (Asp67) and
211 therefore less likely contribute to functional differences between the two systems, the Trp65 motif
212 (**Figure 3e, top**) is structurally different from the corresponding interaction in $HipA_{Ec}$, which has the
213 helix (HipS α3, **Figure S2a**) in a different orientation and a proline residue at this position (**Figure**
214 **3e, bottom**). Moreover, Trp65 is conserved in many HipS orthologues (**Figure S2a**). We
215 hypothesised that placement of the bulky Trp residue inside HipT might block transition of the Gly-
216 rich loop from the outward to the inward conformation, likely required for ATP binding. To test this,
217 we mutated the Trp65 in HipS to alanine and tested the ability of the antitoxin to antagonise the kinase
218 in *E. coli* K-12 on both solid media and in liquid culture (**Figure 3f and S3d**). In both experiments,
219 absence of the bulky Trp65 side chain strongly reduced the antitoxin activity of HipS, confirming that
220 this interaction is critical to inhibition of HipT. We conclude that Trp65 is essential for the ability of
221 HipS to inhibit HipT, presumably either by increasing the affinity of HipS for HipT, or by preventing
222 the Gly-rich loop from adopting the conformation required for ATP binding.

223

224 **The conformation of HipT in the HipBST complex is independent of phosphorylation**

225 In contrast to $HipA_{Ec}$, which undergoes autophosphorylation at a single site (Ser150), HipT was found
226 to harbour two sites in its Gly-rich loop (Ser57 and Ser59), which are subject to autophosphorylation

227 individually but not concomitantly (Vang Nielsen et al., 2019). To understand the individual roles of
228 the two autophosphorylation positions, we next determined crystal structures of two HipBST
229 complexes with HipT serine residues mutated to alanine individually: HipBST^{S57A} (2.4 Å, **Table S1**)
230 and HipBST^{S59A} (3.4 Å). Inspection of the electron densities near the active site revealed that in both
231 cases, the remaining serine residue (i.e. Ser57 in HipBST^{S59A} and Ser59 in HipBST^{S57A}) had become
232 phosphorylated prior to crystallisation (**Figure 4a and S4a-b).** For HipBST^{S59A}, phosphorylation of
233 Ser57 was incomplete and could only be modelled in one of the two HipT molecules in the
234 asymmetric unit (**Figure S4b).** The phosphate group of Ser59 (P-Ser59) forms strong interactions to
235 Lys161, His212, and the catalytic Asp210 inside the active site (**Figure 4a, top**), while P-Ser57 is
236 located further away from the active site and forms hydrogen bonds to Tyr162 and Asp210 (**Figure**
237 **4a, bottom**). In both structures, however, the Gly-rich loop maintains its outward conformation,
238 incompatible with ATP binding, suggesting that HipT is inactive. The phosphate group on Ser59
239 occupies a position very similar to phosphorylated Ser150 in HipA$_{Ec}$, despite the fact that this residue
240 aligns to Ser57 at the sequence level (**Figure S4c, top and 1b**). This position structurally overlaps
241 with the γ phosphate of ATP in the structure of ATP-bound HipA$_{Ec}$, suggesting that phosphorylation
242 prevents nucleotide binding in the kinase active site (**Figure 4b**). Intriguingly, the phosphoryl group
243 of P-Ser57 overlaps structurally with that of phosphorylated Ser147 in HipA$_{So}$, which corresponds to
244 HipA$_{Ec}$ Ser150 at the sequence level (**Figure S4c, bottom**). In order to confirm the phosphorylation
245 state of the HipT variants *in vitro*, we analysed purified HipBST complexes on Phos-tag SDS-PAGE
246 gels, which contain functional molecules that cause retention of phosphorylated protein species in the
247 gel (**Figure 4c, top**). Here, we observed a marked difference in migration between HipT from
248 wildtype HipBST, HipBST^{S59A}, and HipBST^{S57A} confirming that HipT^{S57A} is predominantly
249 phosphorylated while HipT^{S59A} is only partially modified, consistent with the crystal structures.
250 Surprisingly, wildtype HipBST complex is completely non-phosphorylated when purified in this way,
251

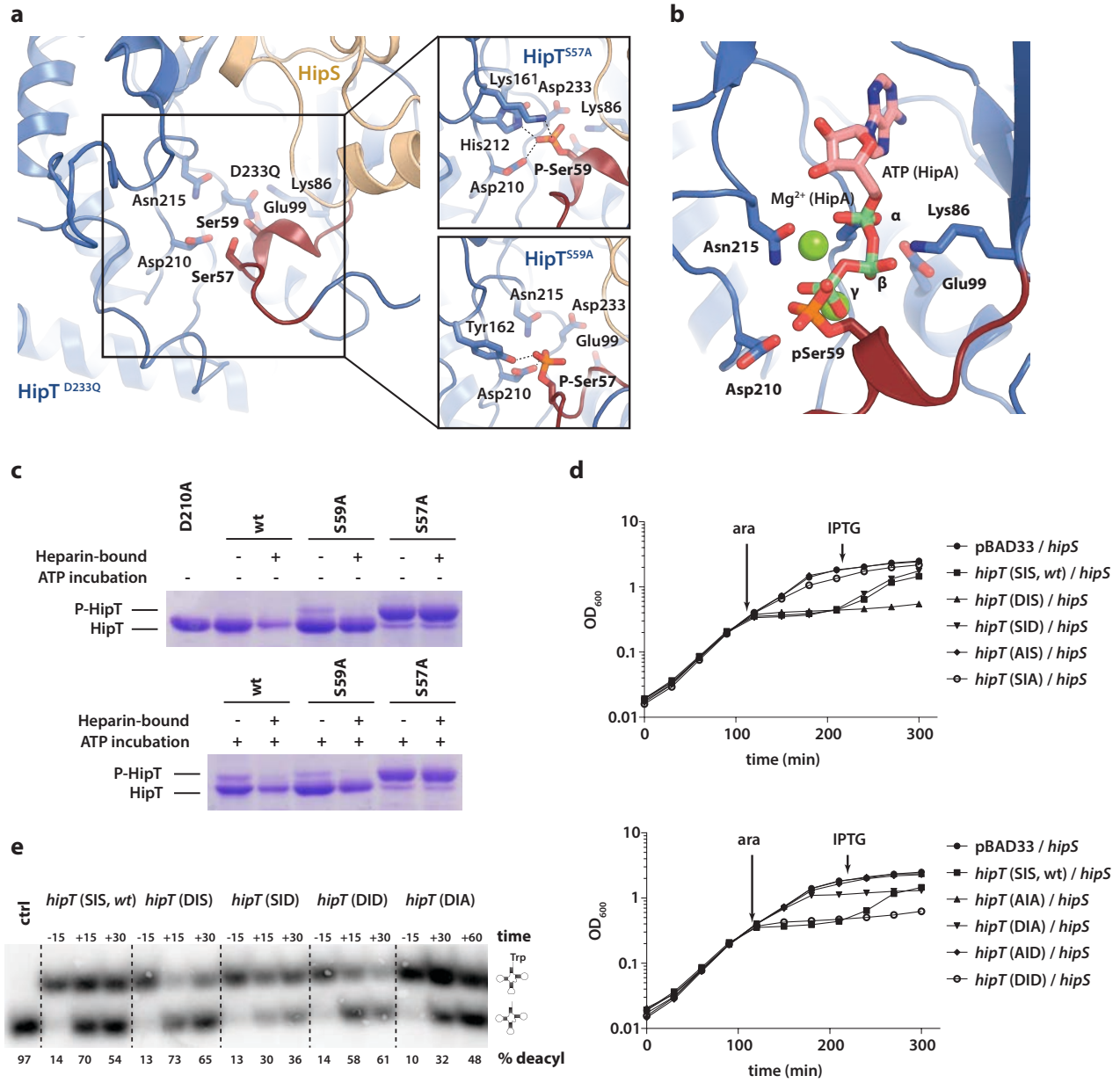

Figure 4. The phosphoserine positions in HipT have distinct functional roles. a. Overview of the HipT kinase active site in the D233Q mutant as well as S57A (top) and S59A (bottom) structures. The phosphate groups on Ser57 (in S59A) and Ser59 (in S57A) are shown in orange and relevant nearby residues are highlighted. **b.** Close-up of the HipT active site as observed for the S57A mutant with relevant active site residues shown as sticks. The Gly-rich loop is shown in red with pSer59 indicated. Overlaid is ATP and 2 Mg^{2+} ions derived from the structure of HipA (PDB: 3DNT, salmon/green) (Schumacher et al., 2009). **c.** HipT bands on Phos-tag gels (stained by Coomassie Blue) of purified HipBST complex before (-) and after (+) a Heparin column step to separate various complex species, as well as before (-) and after (+) treatment with 10 mM ATP, as indicated. Phosphorylated ("P-

261 HipT") and non-phosphorylated ("HipT") protein species are indicated. The gels are representative of two
262 independent experiments. **d.** Top, growth curves measured by OD_{600} of *E. coli* MG1655 harbouring single
263 autophosphorylation mutants pSVN194 (pBAD33::*hipT*^{S57D}, "*hipT* (DIS)"), pSVN195 (pBAD33::*hipT*^{S59D}, "*hipT*
264 (SID)"), pSVN199 (pBAD33::*hipT*^{S57A}, "*hipT* (AIS)"), pSVN201 (pBAD33::*hipT*^{S59A}, "*hipT* (SIA)"), wildtype
265 HipT pSVN1 (pBAD33::*hipT*, "*hipT* (SIS, wt)"), or the empty pBAD33 vector, as indicated, in combination with
266 pSVN109 (pNDM220::*hipS*). *hipT* (ara) and *hipS* (IPTG) expression were induced at the indicated time points. The
267 curves show the mean values of results from at least two independent experiments with error bars indicating standard
268 deviations (hidden when small); Bottom, growth curves of *E. coli* MG1655 harbouring double autophosphorylation
269 mutants pSVN203 (pBAD33::*hipT*$^{S57A+S59A}$, "*hipT* (AIA)"), pSVN205 (pBAD33::*hipT*$^{S57D+S59A}$, "*hipT* (DIA)"),
270 pSVN207 (pBAD33::*hipT*$^{S57A+S59D}$, "*hipT* (AID)"), or pSVN209 (pBAD33::*hipT*$^{S57D+S59D}$, "*hipT* (DID)"), or the
271 empty pBAD33 vector, as indicated, in combination with pSVN109 (pNDM220::*hipS*). *hipT* (ara) and *hipS* (IPTG)
272 expression were induced at the indicated time points. The curves show the mean values of results from at least two
273 independent experiments with error bars indicating standard deviations (hidden when small). **e.** Northern blot
274 analysis probing against $tRNA^{trpT}$ based on RNA extracted from *E. coli* MG1655 harbouring pSVN110
275 (pNDM220::*hipB-S*) in combination with pSVN1 (pBAD33::*hipT*, "*hipT* ($S^{57}IS^{59}$, *wt*)"), pSVN194
276 (pBAD33::*hipT*^{S57D}, "*hipT* ($D^{57}IS^{59}$)"), pSVN195 (pBAD33::*hipT*^{S59D}, "*hipT* ($S^{57}ID^{59}$)"), pSVN209
277 (pBAD33::*hipT*$^{S57D+S59D}$, "*hipT* ($D^{57}ID^{59}$)") or pSVN205 (pBAD33::*hipT*$^{S57D+S59A}$, "*hipT* ($D^{57}IA^{59}$)") at indicated
278 time points in minutes before (-) and after (+) addition of arabinose (0.2%) to induce wildtype *hipT* or
279 autophosphorylation mutants. Quantification of the bands (represented as % deacylated tRNA) is shown below the
280 gel. The control ("ctrl") is chemically deacylated tRNA. The percentage of deacylated tRNA (bottom) was based
281 on quantification of total $tRNA^{trpT}$. Results from strains harbouring pSVN1 (pBAD33::*hipT*), pSVN194
282 (pBAD33::*hipT*^{S57D}), pSVN209 and (pBAD33::*hipT*$^{S57D+S59D}$) are representative of two independent experiments,
283 whereas results from strains harbouring pSVN195 (pBAD33::*hipT*^{S59D}) and pSVN205 (pBAD33::*hipT*$^{S57D+S59A}$) are
284 from single experiments.
285
286

287 but incubation with ATP for 30 minutes leads to a visible increase in phosphorylation of wildtype
288 HipT while no further phosphorylation seemed to take place for the mutants upon incubation with
289 ATP (**Figure 4c, bottom**). In summary, we conclude that the conformation of the HipT active site
290 loop (Gly-rich loop) inside the HipBST complex is independent of the autophosphorylation state.
291

292 **The two phosphoserine positions in HipT have separate functional roles**

293 We next sought to understand the functional implications of autophosphorylation of HipT at the two
294 positions. To this end, we designed a set of HipT mutants with either Ala (to prevent
295 autophosphorylation) or Asp (to mimic the phosphorylated state) in one or both of the two Ser
296 positions. Liquid culture assays showed that both wildtype HipT $S^{57}IS^{59}$ and HipT $S^{57}ID^{59}$ caused
297 growth inhibition upon overexpression in *E. coli* K-12 and could be repressed by concomitant
298 expression of HipS (**Figure 4d, top**) (Vang Nielsen et al., 2019). In contrast to this, growth inhibition
299 by the HipT $D^{57}IS^{59}$ variant could not be repressed upon induction of HipS. Moreover, mutation to
300 alanine at either position caused very little ($S^{57}IA^{59}$) or no ($A^{57}IS^{59}$) growth inhibition, suggesting that
301 the serine residues or their phosphorylated counterparts are important for HipT activity on the target
302 TrpS (**Figure 4d, top**). To rule out any effects of autophosphorylation of the non-mutated Ser
303 position, we created double mutants for which both serine residues were mutated into either alanine
304 or aspartate (**Figure 4d, bottom**). Of these, HipT $D^{57}ID^{59}$ causes immediate growth inhibition while
305 HipT $D^{57}IA^{59}$ shows a similar but delayed phenotype, and consistent with the observation above,
306 neither could be repressed by HipS induction. And as before, placing alanine at either position either
307 completely abolished ($A^{57}IA^{59}$ and $A^{57}ID^{59}$) or strongly delayed ($D^{57}IA^{59}$) growth inhibition. To rule
308 out any effects due to the fact that HipB is missing in this setup, we finally repeated the experiments
309 with concomitant induction of both HipB and HipS and obtained very similar results (**Figure S4d**
310 **and S4e**).

311

312 To confirm that the growth inhibition observed was in fact due to phosphorylation and inactivation
313 of TrpS, we took samples from *E. coli* cultures both before and at several time points after induction
314 of wildtype HipT as well as all variants that caused markedly growth inhibition, extracted total RNA,
315 and performed Northern blotting using probes against $tRNA^{trpT}$ (**Figure 4e**) as well as $tRNA^{gltTUVW}$
316 and $tRNA^{argVYZQ}$ (**Figure S4f**) as controls. Here, charging of the tRNA is visible as a shift of the
317 probed RNA band and thus allows direct assessment of the activity of TrpS *in vivo* in the presence of
318 the various HipT variants. Induction of all variants caused accumulation of deacylated $tRNA^{trpT}$
319 (**Figure 4e**) but no accumulation of the two control tRNAs (**Figure S4f**), which strongly suggests
320 that the observed growth effects are due to reduction in the cellular pool of acylated tRNA. Taken
321 together, we conclude that HipT autophosphorylation at Ser57 prevents HipS inhibition and does not
322 prevent phosphorylation of the target, TrpS. On the other hand, phosphorylation at Ser59 does not
323 affect HipS inhibition, indicating that phosphorylation at the two positions serve separate, functional
324 roles.

325

326 ***hipB* is both required and sufficient for transcriptional repression**

327 To understand the functional role of HipB, specifically how DNA binding has been separated from
328 the antitoxin function in the tripartite *hipBST* system, we initially constructed a vector-based
329 transcriptional fusion reporter, in which the native *hipBST* promoter region and 5' region of the *hipB*
330 gene was transcriptionally fused to *lacZ* (**Figure 5a, right**). We then expressed various combinations
331 of *hipB*, *hipS*, and *hipT* in *trans* in *E. coli* MG1655 Δ*lacIZYA* cells that do not harbour the *hipBST*
332 operon, utilising two inactivating kinase mutations, $hipT^{D210Q}$ (**Figure 5a, left**) and $hipT^{D233Q}$ (**Figure**
333 **S5a**) to avoid toxicity. In both cases, in the absence of expressed *hipBST* components, active
334 transcription could be observed by the blue colour of the colonies (**Figure 5a, left**, top row, pBAD33),

335

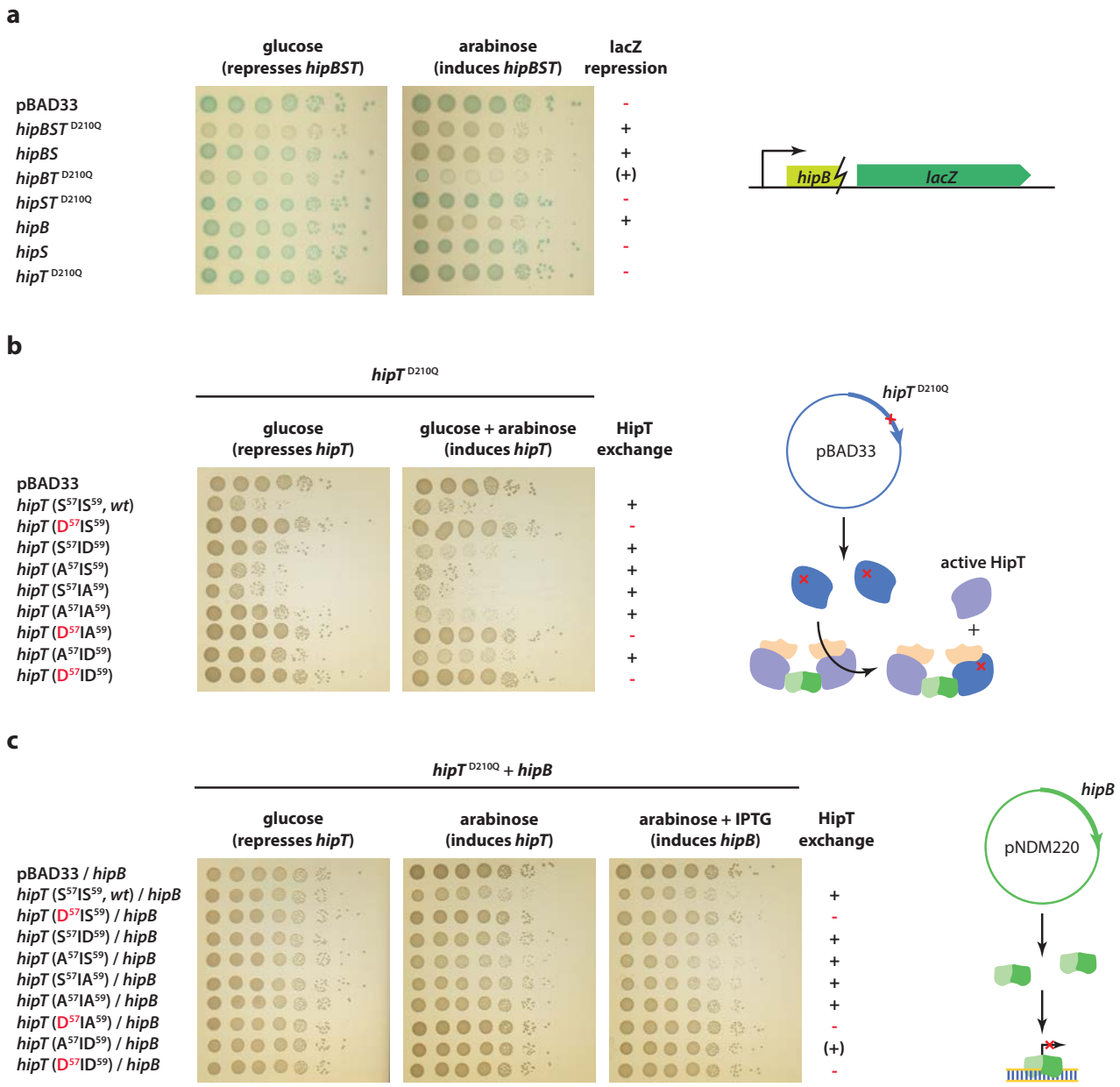

Figure 5. The HipBST complex is dynamic *in vivo*. a. Right, transcriptional reporter assay using a plasmid with the *hipBST* promoter region and a 5' fragment of the *hipB* gene (including 224 bp upstream of *hipB* plus the first 73 bp of the *hipB* gene, shown with a lightening symbol) transcriptionally fused to *lacZ*. Left, *E. coli* TB28 harbouring the reporter plasmid (pSVN141, pGH254::P_{hipBST}-*hipB*'-*lacZ*) and empty pBAD33 vector or combinations of *hipB*, *hipS*, and *hipT* in the context of the HipT^{D210Q} inactive mutant; pSVN180 (pBAD33::*hipB-S-T*^{D210Q}, "*hipBST*^{D210Q}"), pSVN182 (pBAD33::*hipB-S*, "*hipBS*"), pSVN184 (pBAD33::*hipB-T*^{D210Q}, "*hipBT*^{D210Q}"), pSVN187 (pBAD33::*hipS-T*^{D210Q}, "*hipST*^{D210Q}"), pSVN189 (pBAD33::*hipB*, "*hipB*"), pSVN190 (pBAD33::*hipS*, "*hipS*"), or pSVN192 (pBAD33::*hipT*^{D210Q}, "*hipT*^{D210Q}") were grown, diluted, and spotted onto YT, X-gal agar plates

containing 0.2% glucose (to repress *hipB*/*S*/*T*^{D210Q}), or 0.2% arabinose (to induce *hipB*/*S*/*T*^{D210Q}). Results are representative of two independent experiments. **b.** Left, HipT exchange assay where overexpression of a catalytically inactive kinase (HipT^{D210Q}) is used to exchange wild type HipT from the HipBST complex *in vivo*. Right, spot assays of *E. coli* O127 harbouring the empty pBAD33 vector, pSVN220 (pBAD33::*hipT*^{D210Q}, "*hipT* (S^{57}IS^{59}, *wt*)"), pSVN221 (pBAD33::*hipT*$^{S57D+D210Q}$, "*hipT* (D^{57}IS^{59})"), pSVN222 (pBAD33::*hipT*$^{S59D+D210Q}$, "*hipT* (S^{57}ID^{59})"), pSVN223 (pBAD33::*hipT*$^{S57A+D210Q}$, "*hipT* (A^{57}IS^{59})"), pSVN224 (pBAD33::*hipT*$^{S59A+D210Q}$, "*hipT* (S^{57}IA^{59})"), pSVN225 (pBAD33::*hipT*$^{S57A+S59A+D210Q}$, "*hipT* (A^{57}IA^{59})"), pSVN226 (pBAD33::*hipT*$^{S57D+S59A+D210Q}$, "*hipT* (D^{57}IA^{59})"), pSVN227 (pBAD33::*hipT*$^{S57A+S59D+D210Q}$, "*hipT* (A^{57}ID^{59})") or pSVN228 (pBAD33::*hipT*$^{S57D+S59D+D210Q}$, "*hipT* (D^{57}ID^{59})") on YT agar plates containing 0.2% glucose (to repress *hipT*^{D210Q} autophosphorylation mutants) or 0.2% glucose plus 0.2% arabinose to induce a limited amount of HipT. The column to the right indicates whether HipT exchange has taken place (+) or not (-). Results are representative of two independent experiments. **c.** As **b** but with additional overexpression of *hipB* to avoid renewed transcription. Overnight cultures of *E. coli* O127 harbouring pSVN111 (pNDM220::*hipB*) in combination with the empty pBAD33 vector, pSVN211 (pBAD33::*hipT*^{D210Q}, "*hipT* (S^{57}IS^{59}, *wt*)"), pSVN212 (pBAD33::*hipT*$^{S57D+D210Q}$, "*hipT* (D^{57}IS^{59})"), pSVN213 (pBAD33::*hipT*$^{S59D+D210Q}$, "*hipT* (S^{57}ID^{59})"), pSVN214 (pBAD33::*hipT*$^{S57A+D210Q}$, "*hipT* (A^{57}IS^{59})"), pSVN215 (pBAD33::*hipT*$^{S59A+D210Q}$, "*hipT* (S^{57}IA^{59})"), pSVN216 (pBAD33::*hipT*$^{S57A+S59A+D210Q}$, "*hipT* (A^{57}IA^{59})"), pSVN217 (pBAD33::*hipT*$^{S57D+S59A+D210Q}$, "*hipT* (D^{57}IA^{59})"), pSVN218 (pBAD33::*hipT*$^{S57A+S59D+D210Q}$, "*hipT* (A^{57}ID^{59})") or pSVN219 (pBAD33::*hipT*$^{S57D+S59D+D210Q}$, "*hipT* (D^{57}ID^{59})") were grown, diluted, and spotted onto YT agar plates containing 0.2% glucose (to repress *hipT* variants), 0.2% arabinose (to induce *hipT* variants) or 0.2% arabinose and 500 µM IPTG (to induce *hipB*). Results are representative of two independent experiments.

367 while induction of any construct containing *hipB* efficiently repressed transcription (**Figure 5a, left**,
368 right plate, *hipBST*^{D210Q}, *hipBS*, *hipBT*^{D210Q}, and *hipB*). For *hipBST* and *hipBT*, leaky expression on
369 repressing glucose plates was sufficient to reduce transcription. We conclude that *hipB* is both
370 sufficient and required for transcriptional repression of the *hipBST* locus. Given that the *hipBST* and
371 *hipBT* constructs repress transcription even in the absence of inducer, our data are also consistent
372 with HipT (and possibly HipS) stabilising DNA interaction by HipB, as observed for many toxin-
373 antitoxin systems (Harms et al., 2018).
374
375 **Phosphorylation of HipT Ser57 prevents HipS binding *in vivo***
376 In principle, the observed lack of HipS antitoxin inhibition of toxicity in the S57D phosphomimetic
377 HipT mutants could be caused by either lack of binding of HipS or hyperactivity of the kinase. To
378 distinguish between these two scenarios, we next tested if inactive HipT can exchange with wildtype
379 HipT inside the HipBST complex *in vivo* in *E. coli* O127:H6. To achieve this, we constructed a series
380 of HipT autophosphorylation variants on a background of inactive HipT^{D210Q} and asked if expression
381 would release wildtype HipT from endogenous HipBST complexes encoded by *hipBST* of *E. coli*
382 O127:H6 and thus cause toxicity (**Figure 5b, right**). Both in the absence and presence of the inducer
383 arabinose, all inactive HipT autophosphorylation variants, except those harbouring the
384 phosphomimetic Asp57 ($D^{57}IS^{59}$, $D^{57}IA^{59}$, and $D^{57}ID^{59}$) were able to induce toxicity in this setup,
385 thus suggesting that exchange can take place when Ser57 is not phosphorylated (**Figure 5b, left**). Of
386 these, the $S^{57}IS^{59}$, $A^{57}IS^{59}$, and $S^{57}IA^{59}$ variants had the strongest ability to release wildtype HipT
387 activity while the $S^{57}ID^{59}$, $A^{57}IA^{59}$ and $A^{57}ID^{59}$ variants activated HipT at a lower level. To exclude
388 the possibility that expression of inactive HipT would affect the natural transcriptional repression of
389 the endogenous HipBST complex, we repeated the experiment in a setup where excess HipB is
390 expressed from a separate plasmid using IPTG, knowing that this represses transcription (**Figure 5c,**

391 **right**). Due to an uncharacterised growth inhibiting effect observed upon *hipBT* co-expression for the
392 inactivating kinase mutations, *hipT*^{D210Q} (**Figure 5a, left**) and *hipT*^{D233Q} (**Figure S5a**), we used
393 genetic constructs with a lower expression level of the HipT mutants for expression in combination
394 with HipB to obtain the data in figure 5c. Here we found similar results even with full transcriptional
395 repression, supporting that the observed toxicity is indeed due to wildtype HipT being exchanged
396 away from preformed endogenous HipBST complexes upon expression of inactive toxin. To confirm
397 that the growth defects observed were in fact dependent on the *hipBST* system and not a secondary
398 effect in the host, we performed a similar assay in *E. coli* K-12 with the intact *hipBST* operon fused
399 to *lacZ* encoding wildtype HipT (**Figure S5b**). Growth inhibition was only observed when inactive
400 HipT$^{D210Q/D233Q}$ was expressed *in trans* confirming that the phenotype is indeed dependent on the
401 *hipBST* operon. To ensure that the low expression levels of the HipT^{D210Q} autophosphorylation
402 mutants in combination with HipB was not in themselves causing the observed growth inhibitions as
403 seen for high expression levels (**Figure 5a, left and S5a**), we finally transformed the same vectors
404 used in *E. coli* O127:H6 into *E. coli* K-12. None of the vectors caused growth inhibition upon
405 induction (**Figure S5f**), confirming that the phenotype observed in **Figure 5b** must be due to the
406 presence of the native *hipBST* operon. Finally, to rule out any differences in transcription of the
407 *hipBST* promoter between *E. coli* K-12 and O127:H6, we confirmed that mRNA expression can be
408 repressed in *E. coli* K-12 when *hipBST*^{D210Q} is present *in trans* (**Figure S5c**) and that the
409 transcriptional start sites (TSS) in the two strains are identical (**Figure S5d-e**). In summary, we
410 conclude that free HipT molecules are able to exchange with those inside the inhibited HipBST
411 complex, except in the S57D mutants, suggesting that phosphorylation at Ser57 controls exchange,
412 likely via control of binding of HipS.
413
414 **The core HipT kinase domain is flexible in solution**

415 Since the protein exchange experiments suggested that the HipBST complex is dynamic *in vivo*, we
416 finally performed a careful analysis of the obtained small-angle X-ray scattering (SAXS) data to
417 understand the structure of the complex in solution (**Figure S6a-b**). We found, that the pair distance
418 distribution function indicates a maximum complex diameter of 170 Å, significantly larger than the
419 value calculated from the crystal structure (140 Å) suggesting some degree of structural flexibility
420 (**Figure S6c-d**). Moreover, fitting of the crystal structure to the solution data yielded a relatively poor
421 fit, so to accommodate internal flexibility, the HipT structure was split into three parts, roughly
422 corresponding to the N-terminal mini domain (1-59), the N-terminal subdomain 2 (60-169), and the
423 core kinase domain (170-335) (**Figure 2a**). Following rigid body refinement against the SAXS data
424 with soft restraints between the three parts of HipT, including HipS and HipB, and imposing two-fold
425 symmetry, we obtained a better fit which could be further improved by allowing for partial
426 dimerisation of the hetero-hexamer (see Material and Methods for details). In this model, the core
427 kinase domain of HipT has a looser structure than observed in the crystal structure (root mean square
428 deviation for Cα atoms HipT ~6.5 Å, HipBST ~7 Å) suggesting that the complex in the solution state
429 allows for internal flexibility in the kinase. In summary, in solution structural analysis confirms that
430 the HipBST complex has a flexible structure, likely caused by structural dynamics in the HipT core
431 kinase domain, thus consistent with a model in which HipS (and perhaps HipB) can release and rebind
432 HipT dynamically.
433
434 **DISCUSSION**
435 In this paper, we present a detailed structural and functional analysis of the tripartite HipBST toxin-
436 antitoxin system from enteropathogenic *E. coli* O127:H6. We show that most HipT kinases contain a
437 conserved SIS motif in their Gly-rich loops, allowing for fine-tuned regulation via dual auto-
438 phosphorylation. Other members of the family contain various combinations of Ser and Thr at these

439 positions, which may serve similar roles since Hip toxins are Ser/Thr kinases (Pereira et al., 2011).
440 Crystal structures of the HipBST complex in several, naturally occuring phosphorylation states
441 demonstrate that HipT is found in its inactive state inside the HipBST complex regardless of its
442 autophosphorylation state, consistent with a model whereby HipS, possibly aided by the DNA-
443 binding protein HipB, keeps the kinase in an inactive conformation and thus overrules any effects of
444 autophosphorylation. We show that this inhibition is dependent on a conserved Trp65 in HipS, which
445 couples HipS binding directly to the active site of HipT and the conformation of its Gly-rich loop.
446 Trp65 is located in a motif that differs both structurally and at the sequence level from the
447 corresponding region in the N-terminal subdomain 1 of HipA, which is otherwise very similar to
448 HipS (Gerdes et al., 2021). Together, this suggests that the molecular basis for the role of HipS as
449 antitoxin in the HipBST complex involves prevention of the Gly-rich loop from transitioning from
450 the outward, inactive state, to another conformation compatible with ATP binding (**Figure 6**).
451

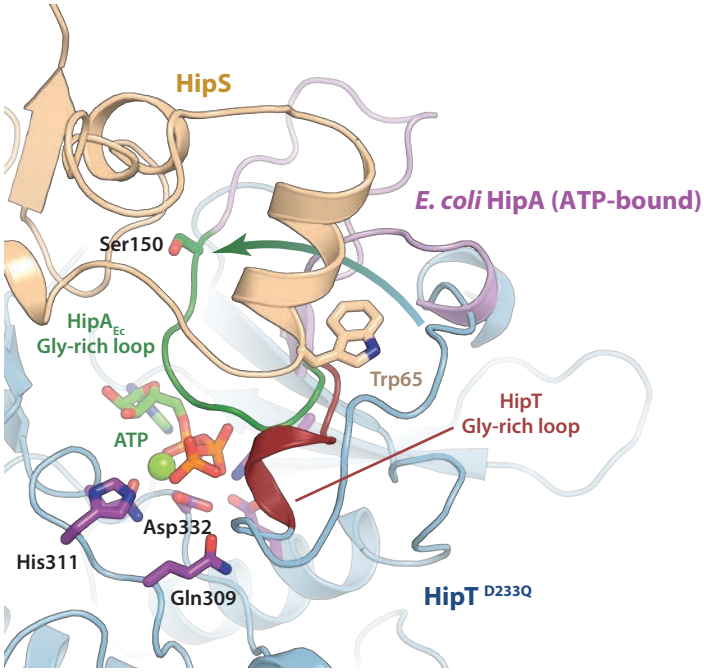

Figure 6. Model for the action of HipS as antitoxin in the HipBST system. Structural comparison of the positions of the Gly-rich loops in HipT D233Q (blue) and *E. coli* K-12 HipA in its ATP-bound conformation (PDB: 3DNT, green/purple) (Schumacher et al., 2009). Shown is also HipS with Trp65, which is predicted to prevent transition of the Gly-rich loop from an outward-facing (HipT) to an inward-facing (HipA:ATP) conformation (shown with an arrow). The active site residues of HipA as well as ATP:Mg^{2+} are shown with sticks on top of the HipT cartoon. Ser150, which undergoes phosphorylation in HipA, is indicated as well.

461 The size and topology of the HipT kinase with its lack of the N-terminal subdomain 1 found in HipA
462 is reminiscent of the Cyclin-dependent kinases (Cdks), which are minimal kinases that regulate the
463 eukaryotic cell cycle (**Figure S7a**) (Lim & Kaldis, 2013). Intriguingly, one of these, Cdk5, also
464 regulates translation through direct phosphorylation of glutamyl-prolyl tRNA synthetase (EPRS)
465 (Arif et al., 2011). Despite differences in tertiary structure (**Figure S7b**), the residues involved in the
466 active site align well, suggesting common reaction mechanisms. Cyclin-dependent kinases are
467 stabilised by two hydrophobic regions, the R (regulatory) and C (catalytic) spine (Taylor & Kornev,
468 2011). Of these, the R spine changes conformation upon an activating phosphorylation by flipping
469 the final active site residue into place and stabilising the kinase by forming an interaction to an
470 aspartate residue in the so-called F helix (Baugh et al., 2015). While several of these structural
471 elements are not present in HipT, the bacterial kinase does feature a conserved hydrophobic core
472 similar to the C spine (**Figure S7c-e**). These regions are more extended than seen in Cdk, in particular
473 due to the presence of two additional, conserved aromatic residues (Y138 and Y232 in HipT, **Figure**
474 **S7d-e**). In the structure of ATP-bound HipA, the adenine base intercalates right between these and
475 thereby connects the N and C lobes of the kinase. Interestingly, the invariant small hydrophobic
476 residue found between the phosphor-serine positions in HipT (S<u>I</u>S) would connect the adenine base
477 to the N lobe, suggesting that it is conserved to preserve the ATP binding. In general, it thus appears
478 that the similarities between bacterial and eukaryotic kinases may be larger than hitherto appreciated
479 and consequently, that the vast set of knowledge available for the eukaryotic enzymes might help us
480 understand the Hip kinases as well.
481
482 A surprising discovery of this study is that HipT was found with phosphorylation at Ser57 or Ser59
483 when expressed in the context of the inactive HipBST complex. This suggests that some active (HipS-
484 free) HipT exists in the cell and hence compatible with a model whereby the HipBST complex is

485 dynamic and allows HipT to dissociate *in vitro*. In this context, it is likely that the exposed
486 conformation of the Gly-rich loop renders it particularly susceptible to phosphorylation by active
487 HipT kinase. Taken one step further, this could indicate that a secondary effect of HipS binding (apart
488 from inactivating the kinase) is to expose the kinase to regulation via autophosphorylation in *trans*.
489 We still don't understand what controls whether HipT becomes modified at one or the other position
490 but the structures of $HipT^{S57A}$ and $HipT^{S59A}$ could suggest that subtle changes in the loop can make a
491 big difference (**Figure 4a**). Moreover, since Ser57/Ser59 phosphorylation was observed for both
492 alanine single mutations *in vitro*, the presence of both serine residues does not appear to be important
493 for the autophosphorylation activity of HipT. Finally, the observation that the $S^{57}IS^{59}$, $A^{57}IS^{59}$, and
494 $S^{57}IA^{59}$ $HipT^{D210Q}$ variants exhibit a stronger toxicity due to exchange with wildtype HipT than the
495 $A^{57}IA^{59}$ variant *in vivo* (**Figure 5b-c**) indicates that the hydroxyl groups of the serine residues play a
496 role in the binding of HipS.
497
498 Intriguingly, although the two autophosphorylation positions in HipT occupy a similar space near the
499 γ-phosphate of ATP, they serve different roles. HipT is active in both phosphomimetic isoforms ($S^{57}D$
500 and $S^{59}D$) while removal of the hydroxyl group on either serine by mutation to alanine ($S^{57}IA^{59}$,
501 $A^{57}IS^{59}$ and $A^{57}IA^{59}$) reduces its ability to cause growth inhibition. In contrast to this, we found that
502 both $S^{57}IA^{59}$ and $A^{57}IS^{59}$ remained capable of autophosphorylation, suggesting that the presense of
503 both of the serine residues or their phosphorylated counterparts could be important for regulating
504 whether HipT is active on itself or its target (TrpS). Taken together, these results are consistent with
505 a model in which autophosphorylation at either position is required for target phosphorylation.
506 Surprisingly, in contrast to the $A^{57}ID^{59}$ mutant, the $D^{57}IA^{59}$ mutant was still active in inhibiting growth
507 (but with a delayed effect compared to $D^{57}IS^{59}$, $S^{57}ID^{59}$, and $D^{57}ID^{59}$), suggesting that
508 phosphorylation of Ser57 results in a kinase, which is more potent against its target compared to

509 phosphorylation of Ser59. Finally, although the $D^{57}ID^{59}$ mutant is fully active in growth inhibition,
510 this may be artificial, as dual phosphorylation has not been observed *in vivo* (Vang Nielsen et al.,
511 2019). Nevertheless, the $D^{57}ID^{59}$ mutant gives us valuable information, as it shows that growth
512 inhibition does not require the presence of a serine residue and that phosphorylation is likely what
513 determines the active state. The differences in the ability of the $S^{57}IA^{59}$ and $D^{57}IA^{59}$ mutants to cause
514 growth inhibition are also striking. The $S^{57}IA^{59}$ mutant has a very small growth inhibitory effect,
515 whereas $D^{57}IA^{59}$ has a clear effect. One explanation for this observation could be that the $S^{57}IA^{59}$
516 mutant has a slower rate of autophosphorylation compared to wildtype ($S^{57}IS^{59}$) and that this would
517 be required for HipT activity. When examining the other autophosphorylation site, Ser59, it is
518 noteworthy, that the $S^{57}ID^{59}$ mutant is fully active, while the $A^{57}IS^{59}$ and $A^{57}ID^{59}$ mutants are inactive.
519
520 Another question raised by the structures is how HipS can be bound in the complex with Ser57 in its
521 phosphorylated state if this serves to block HipS binding? In this context, it is important to note,
522 however, that only a minor fraction of the purified complex is phosphorylated (**Figure 4c**),
523 confirming that if HipT (Ser57-P) binds to HipS at all, it probably binds very poorly. It is also possible
524 that phosphorylation occurred during purification. In either case, we believe that our data is
525 compatible with the model for DNA binding and toxin activation for the HipT kinase toxin shown in
526 **Figure 7**. Under non-activating conditions, HipBST will be repressing the *hipBST* operon via binding
527 to promoter DNA. Liberation of HipBST from DNA by an unknown mechanism will result in relaxed
528 promoter repression and increased transcription from the operon. Free HipT could then form three
529 populations, non-phosphorylated HipT, HipT P-Ser57, and HipT P-Ser59. Our results indicate that
530 both phosphorylated forms are active on TrpS and as a result of this, reduce cell growth. Furthermore,
531 HipT P-Ser59 would readily be able to (re-)bind HipS, and therefore form a stable and inactive
532 HipBST complex as well as tightly bind the *hipBST* promoter, effectively shutting down the kinase
533

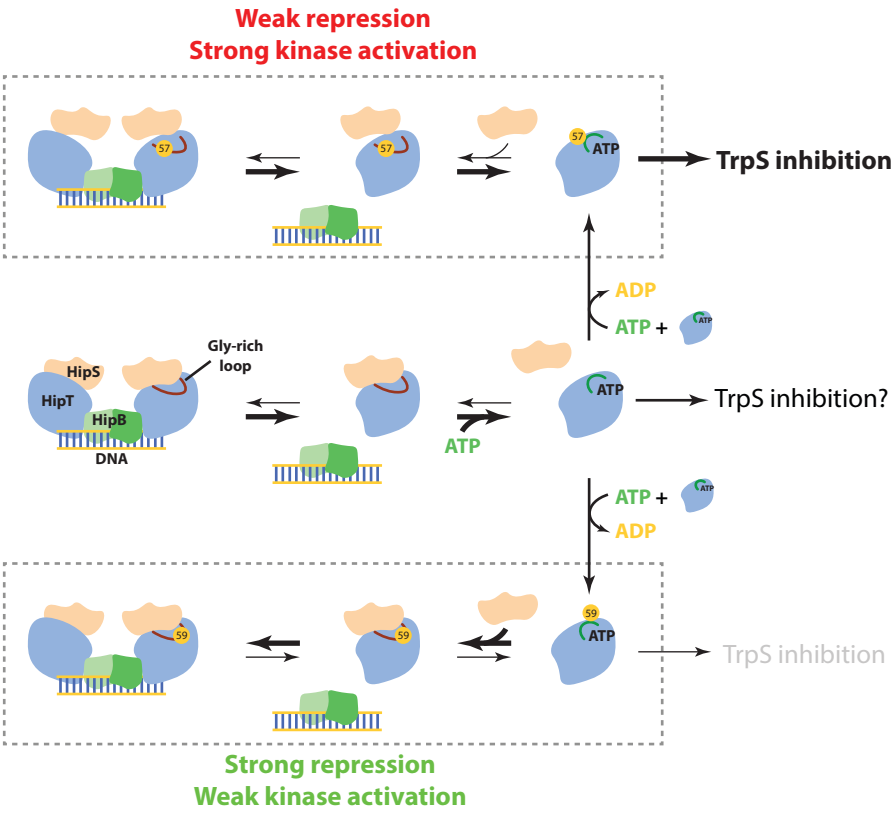

Figure 7. Proposed model of regulation and activation of the HipBST system. Transcription from the *hipBST* operon (middle row, left) is repressed by binding of the HipBST hetero-hexamer in which HipT is inactive and the Gly-rich loop (red) is outward-facing when HipS is bound. The dynamic HipBST complex can disassociate to generate free HipT, which can phosphorylate another HipT kinase and perhaps TrpS, using ATP. Autophosphorylation at Ser 57 (top box) severely reduces HipS binding, thereby prolonging the growth inhibitory effect of HipT by keeping the kinase active and preventing full transcriptional repression. On the contrary, autophosphorylation at Ser59 (bottom box) stabilises HipS binding and the HipBST complex, reducing the activity of HipT on TrpS compared to when autophosphorylated at Ser57 and repressing transcription from the *hipBST* operon.

544 activity, halting the expression of new protein. On the contrary, HipT P-Ser57 would have reduced
545 HipS binding and therefore stay in its active conformation. The overall effect on growth could then
546 be a balance between these two counter-acting responses.
547

548 **ACKNOWLEDGEMENTS**

549 The authors are indebted to the beamline staff at P14 in EMBL Hamburg, and BioMAX in MaxIV
550 Lund for help during data collection. This project was funded by grants from the Novo Nordisk
551 Foundation (NNF18OC0030646 to D.E.B.) and Danish Natural Research Foundation's Centre of
552 Excellence for Bacterial Stress Response and Persistence (grant number DNRF120).
553

554 **COMPETING INTERESTS**

555 The authors confirm that there are no competing interests.
556

557 **AUTHOR CONTRIBUTIONS**

558 Conceptualization, K.G., M.A.S, and D.E.B.; Investigation, R.L.B., S.V.N., F. B., and J.L.; Formal
559 Analysis, R.L.B, S.V.N., F.B., and J.S.P; Writing – Original Draft, R.L.B., S.V.N., and D.E.B.;
560 Writing – Review & Editing, R.L.B., S.V.N., J.L., J.S.P., K.G., M.A.S., and D.E.B; Visualization,
561 R.L.B., S.V.N., M.A.S., and D.E.B.; Funding Acquisition, D.E.B. and K.G.; Resources, J.S.P., K.G.,
562 M.A.S. and D.E.B; Supervision, K.G., J.S.P., M.A.S., and D.E.B.
563

564 **MATERIALS AND METHODS**

565 **Phylogenetic analysis.** The previously identified set of 48 HipT orthologues (Gerdes et al., 2021)
566 was used for sequence alignment by Clustal Omega (Sievers & Higgins, 2018) at www.ebi.ac.uk and
567 imported into Jalview (Waterhouse et al., 2009). The phylogenetic tree was visualized using iTOL

568 (Letunic & Bork, 2019). Reconstruction of the phylogenetic tree was accomplished using IQ-TREE
569 that uses the Maximum Likelihood approach and Ultrafast bootstrapping via the CIPRES module in
570 Genious Prime (Minh et al., 2020).
571
572 **Strains and plasmids.** Strains and plasmids are listed in **Table S2**, and DNA oligonucleotides in
573 **Table S3**.
574
575 **Site-directed mutagenesis.** Amino acid change $HipT_{S57A}$ was constructed by PCR mutagenesis
576 (**Table S3**) as previously performed (Vang Nielsen et al., 2019). PCR product was digested with
577 DpnI, and resulting plasmid transformed into *E. coli* strain DH5α.
578
579 **Protein purification and structure determination.** Expression of the *E. coli* O127:H6 HipBST
580 complex was done using constructs pSVN78 ($HipBST_{S57A}$), pSVN96 ($HipBST_{D233Q}$), and pMME3
581 ($HipBST_{S59A}$) derived from pSVN78. The constructs contained the genes coding for HipB, HipS, and
582 C-terminal hexa-histidine tagged HipT, all separated, and with optimised Shine-Dalgarno sequences
583 for large scale expression. All constructs contained an IPTG-inducible promoter and ampicillin
584 resistance gene for selection. For each construct, 2 L cultures with a cell density of $OD_{600} = 0.6$ were
585 induced with a final concentration of 1 mM IPTG, and left to express ON at 20°C. Cell pellets were
586 resuspended in lysis buffer (50 mM Tris-HCl, pH 7.5, 300 mM NaCl, 20 mM imidazole, 5% glycerol,
587 5 mM BME) together with 1 mM PMSF. Cells were lysed by sonication and the cleared lysate was
588 applied to a 5 mL HisTrap HP column (Cytiva) equilibrated in lysis buffer, and washed in wash buffer
589 (50 mM Tris-HCl, pH 7.5, 300 mM NaCl, 40 mM imidazole, 5 mM BME), before eluting with elution
590 buffer (50 mM Tris-HCl, pH 7.5, 300 mM NaCl, 400 mM imidazole, 5 mM BME). The eluate was
591 applied directly to a 5 mL Heparin HF column equilibrated in 70% Buffer A (50 mM Tris-HCl, pH

592 7.5, 5 mM BME) and 30% Buffer B (50 mM Tris-HCl, pH 7.5, 1M NaCl, 5 mM BME) running on
593 an ÄKTA Pure system (Cytiva). Final separation was achieved after concentrating the Heparin elution
594 to approximately 8 mg/mL using a Vivaspin column with a 30 kDa cutoff (Sartorius), before applying
595 the sample to a Superdex 200 10/300 GL (Cytiva) column equilibrated in gel filtration buffer (20
596 mM Tris-HCl, pH 7.5, 300 mM NaCl, 5 mM BME). Crystals of HipBST^{S57A} grew as clusters of thin
597 plates in a 2 µL drop with a 1:1 ratio of protein to buffer, which consisted of 0.1 M Bicine, pH 9, 8%
598 MPD and with a protein concentration of 5 mg/mL, and a reservoir of 200 µL. Crystals of all three
599 mutant forms were obtained by a very similar protocol. All crystals were cryoprotected in the mother
600 liquor supplemented with 25% MPD before freezing in liquid N_2.
601
602 Data collection for HipBST^{S57A} was performed at P14 in Hamburg and for HipBST^{S59A} and
603 HipBST^{D233Q} at BioMAX in Lund. For HipBST^{S59A} and HipBST^{D233Q}, 7,200 images were collected
604 with an oscillation of 0.1° and a transmission of 100%. The HipBST^{S57A} data set was collected with
605 an oscillation of 0.1°, 3,600 images and a transmission of 70%. All data was processed in XDS
606 (Kabsch, 2010), using the CC½ value after scaling as indicator of the data resolution limit (Karplus
607 & Diederichs, 2012). The space group was confirmed using Pointless (Evans, 2006), and all structures
608 were determined using molecular replacement with Phaser (McCoy et al., 2007) from the CCP4 suite
609 (Winn et al., 2011). The data set for HipBST^{S57A} used a heavily truncated HipA to obtain initial phases
610 for HipT, while the data set for HipBST^{S59A} and HipBST^{D233Q} used the solved structure of HipBST
611 as a search model. Refinement was performed using Buster (Smart et al., 2012) using 1 big cycle of
612 20 small cycles of refinement when building, and 5 big cycles of 100 small cycles of refinement
613 afterwards. Non-crystallographic symmetry (NCS) restraints were used during building since the
614 asymmetric unit (ASU) contained a dimer but some refinement rounds without NCS were also
615 included to allow for differences between the molecules in the ASU. Automatic water placement was

616 used and water molecules with no density were removed. Model building was performed in Coot
617 (Emsley et al., 2010). All structures were validated by the MolProbity server and Rama-Z scores.
618 Final R-work/R-free for $HipBST_{D233Q}$, $HipBST_{S57A}$, and $HipBST_{S59A}$, is 0.19/0.23, 0.21/0.24, and
619 0.20/0.24, respectively.
620
621 **Phos-tag gel of pre- and post-incubation with ATP.** 15% Phos-tag acrylamide gels (Wako) were
622 cast according to the manufacturer's guidelines, except that 100 μM Phos-tag acrylamide was used to
623 ensure proper separation between phosphorylated and non-phosphorylated HipT. The non-
624 phosphorylated HipT control was expressed from pSNN2. The gel was run at 4 °C until the loading
625 dye reached the bottom of the gel and visualized using standard Coomassie Blue staining as for
626 normal SDS-PAGE gels. HipBST samples were run directly on the gel orincubated with ATP for 30
627 minutes at room temperature in a final mixture of: 2 mM KCl, 3.2 μM $ZnSO_4$, 4 mM $MgCl_2$, 66 μM
628 ATP, 14 μL gel filtration buffer, and 1 mg/mL protein sample.
629
630 **Spot assays and growth curves.** Cultures were grown in liquid YT medium or MOPS minimal
631 medium + 0.2% glucose at 37°C shaking at 160 rpm and solid medium used was YT agar plates,
632 which were incubated at 37°C for approximately 16 h. When applicable, media were supplemented
633 with 25 μg/mL chloramphenicol, 30 μg/mL ampicillin, 25 μg/mL kanamycin and/or 40 μg/mL 5-
634 bromo-4-chloro-3-indolyl-β-D-galactopyranoside (X-gal). For spot assays, cells were grown as
635 overnight cultures, diluted to obtain the same values of OD_{600}, centrifuged at 5,000 rpm for 5 min,
636 washed in phosphate-buffered saline (PBS), and serially diluted before being spotted onto YT agar
637 plates containing the indicated amount of inducer/repressor. Gene expression from plasmids carrying
638 the pBAD promoter was induced by a final concentration of 0.2% arabinose and repressed by 0.2%
639 glucose. Gene expression from plasmids carrying the $P_{A1/O4/O3}$ promoter was induced by a final

640 concentration of 200 or 500 μM isopropyl-D-1 thio-galactopyranoside (IPTG), as indicated. Growth
641 experiments were done in YT medium with addition of relevant antibiotics, diluted from overnight
642 cultures and grown exponentially for at least 4 h until a seemingly constant doubling time. At OD_{600}
643 ≈ 0.2, arabinose (0.2%) was added to induce wildtype *hipT* or autophosphorylation mutants. After
644 another 1.5 h, IPTG (200 μM) was added to induce *hipS* or *hipBS*. For each repetition, an independent
645 colony from the strain was used to start separate cultures. No outliers were rejected.
646
647 **Northern blot analysis.** Total RNA samples were prepared using hot phenol extractions. Cultures
648 were grown in YT medium (or MOPS minimal medium + 0.2% glucose in the case of the *E. coli*
649 TB28 strain used for primer extension as described below). At indicated time points 10 mL were
650 harvested into 1.25 mL ice-cold stop solution (5% phenol, pH 4.3 in absolute ethanol) and pelleted
651 by centrifugation at 4,000 rpm at 4 ºC for 10 min. Cell samples were resuspended in 200 μL ice-cold
652 solution I (0.3 M sucrose; 0.01 M Na-Acetate, pH 4.5) and mixed with 200 μL solution II (2% SDS;
653 0.01 M Na-Acetate, pH 4.5) and 400 μL phenol (pH 4.3). Samples were vortexed for 10 s. before
654 incubation at 65 ºC for 3 min. followed by freezing in liquid nitrogen and centrifugation at 13,000
655 rpm at room temperature for 5 min. The upper phase was transferred to a new tube with 400 μL
656 phenol (pH 4.3) followed by another round of the vortexing, heating, freezing and centrifugation
657 steps. The RNA was precipitated in 1 mL ice-cold absolute ethanol and 50 μL RNA storage buffer (3
658 M Na-Acetate, pH 4.7; 10 mM EDTA) at -80 ºC for a minimum of 30 min. RNA was then pelleted
659 by centrifugation at 13,000 rpm at 4 ºC for 30 min., washed in 70% ice-cold ethanol and air-dried at
660 room temperature. Finally, samples used for northern blotting analysis were resuspended in 20 μL
661 RNA storage buffer, whereas samples used for primer extension were resuspended in 20 μL nuclease-
662 free water. Deacylated control sample used for northern blotting analysis was prepared by mixing 4
663 μL of any of the total RNA samples with 6 μL 1 M Tris-HCl (pH 9) and 50 μL nuclease-free water

664 and incubating for 2 hours at 37 ºC. This was followed by the addition of 150 µL ice-cold absolute
665 ethanol and 4 µL 5 M NaCl and the tube was incubated at -20 ºC for 15 min. The sample was then
666 centrifuged at 13,000 rpm at 4 ºC for 30 min. The supernatant was discarded, and RNA pellet was
667 air-dried at room temperature and resuspended in 4 µL RNA storage buffer.
668
669 Northern analysis was used for detection and comparison of charged versus uncharged tRNA. 4 µL
670 RNA samples were mixed with 6 µL tRNA loading buffer (0.1 M Na-succinate, pH 5; 8 M urea;
671 0.05% bromophenol blue and 0.05% xylene cyanol) and separated on 6% polyacrylamide gels with
672 8 M urea buffered in 0.1 M Na-succinate (pH 5) and run at 35 V. RNA was transferred to a Hybond-
673 N+ membrane (Amersham) at 550 mA constant for 1 hour in blotting buffer (0.8 M Tris; 40 mM
674 EDTA; acetic acid to pH 8.1). Membranes were pre-hybridized at 42 ºC in 6 mL hybridization buffer
675 (5 x SSPE; 5 x Denhardt's solution; 0.5% SDS; ~0.55 mg/mL herring sperm DNA (Sigma)) for one
676 hour before addition of 10 µM DNA oligonucleotide probe, which had been radioactively labelled
677 with [γ-^{32}P]-ATP, for overnight hybridization. Oligonucleotides complementary to the tRNA
678 anticodons of interest were 5'-end labelled using T4 polynucleotide kinase (Thermo Scientific) and
679 40 µCi of [γ-^{32}P]-ATP (6000 Ci/mmol) by incubating at 37 ºC for 2 hours. For detection of $tRNA^{trpT}$,
680 $tRNA^{gltTUVW}$ and $tRNA^{argVYZQ}$, oligonucleotides CCCAACACCCGGTTTTGG,
681 CCTGTTACCGCCGTGAAAGGG and TCCGACCGCTCGGTTCGTAGC were used, respectively.
682 Excess probe was removed by washing in 2 x SSC buffer with 0.1% SDS at room temperature and
683 radiation was visualized by phosphorimaging. Membranes were stripped for re-probing at 95 ºC in
684 stripping buffer (0.1 x SSPE; 0.5% SDS) until no remaining radiation was detected.
685
686 **Primer extension analysis.** Primer extension was used to map mRNA 5' ends using radioactively
687 labelled primers following extension by reverse transcription. Specific oligonucleotide primers (4

688 pmol) were radioactively 5'-end labelled with 130 µCi of [γ-^{32}P]-ATP (6000 Ci/mmol) using T4
689 polynucleotide kinase (Thermo Scientific) and incubated for 30 min at 37 ºC followed by inactivation
690 for 15 min at 75 ºC and cooling on ice. To remove excess unincorporated [γ-^{32}P]-ATP, the reaction
691 was centrifuged through an illustra MicroSpin G-25 Column (Cytiva) at 750 g for 1 min.
692 Sequencing reactions used as markers of molecular weight were generated using a purified PCR
693 fragment amplified with primers FP43 and RP38 and 0.1 pmol from pKG127 as template DNA. The
694 reactions were incubated with radioactively labelled primer (0.4 pmol) and extensions were
695 performed with DreamTaq DNA polymerase (Thermo Scientific) in the presence of either ddGTP,
696 ddATP, ddTTP or ddCTP termination mix (Roche). PCRs were carried out and reactions were
697 stopped by the addition of an equal volume of 2 x formamide loading buffer (95% formamide; 0.025%
698 bromophenol blue and 0.025% xylene cyanol; 5 mM EDTA; 0.025% SDS).
699
700 For extension reactions, radioactively labelled oligonucleotides (0.2 pmol) were hybridized to 10 µg
701 of total RNA by incubating at 80 ºC for 5 min followed by quick cooling on ice for 5 min. Reverse
702 transcriptions were carried out using Superscript III reverse transcriptase (Invitrogen) in 1 x First-
703 Strand buffer plus 10 mM DTT and 1 mM dNTP for 1 hour at 52 ºC and 47 ºC for RP35 and RP37,
704 respectively. Reactions were stopped by the addition of an equal volume of 2 x formamide loading
705 buffer. Sequencing and extension reactions were fractionated on 6% polyacrylamide gels with 8 M
706 urea, buffered in 1 x TBE and run at 45 W. Resulting gels were fixed in fixing solution (50% ethanol;
707 10% acetic acid), dried and visualized by phosphor imaging. The promoter of *hipBST* was analysed
708 by primer extension using RP35 and RP37 for mapping of the transcriptional start site from pSVN141
709 (pGH254::P$_{hipBST}$-*hipB'-lacZ*) in *E. coli* TB28 and the native *hipBST* operon in *E. coli* O127,
710 respectively.
711

712 **Small-angle X-ray scattering measurements and analysis.** $HipBST_{S57A}$ purified as specified in
713 "Protein purification and structure determination" was used for the SAXS analysis. The SAXS
714 measurements were performed on the optimized NanoSTAR instrument (Bruker AXS) at the iNANO
715 center at Aarhus University (Lyngsø & Pedersen, 2021). It uses a high brilliance Ga metal-jet X-ray
716 source (Excillum), special long optics, a two-pinhole collimation with a home-built 'scatterless' slit
717 pinhole, and a VÅNTEC-2000 (Bruker AXS) microgap 2D gas proportional detector. The sample
718 and buffer were measured in the same flow-through quartz capillary, the scattering from the buffer
719 was subtracted from that of the sample, and the data were converted to absolute scale using the
720 scattering from water. The intensity data, $I(q)$, are displayed as a function of the modulus of the
721 scattering vector $q = 4\pi \sin(\theta)/\lambda$, where 2θ is the scattering angle and λ is the wavelength of the
722 X-rays. The fit to the data in a Guinier plot gave the radius of gyration $R_g = 52.2 \pm 0.2$ Å and the
723 forward scattering $I(0) = 0.0868 \pm 0.005$ cm^{-1}. The molar mass was calculated as: $M =$
724 $I(0)N_A/(c\Delta\rho_m^2)$, where N_A is Avogadro's number, $c = 1.01$ mg mL^{-1} is the mass concentration, and
725 $\Delta\rho_m = 2.00 \times 10^{10}$ cm g^{-1} is the typical excess scattering length per unit mass for proteins. The
726 radius of gyration and forward scattering can also be obtained from the pair distance distribution
727 function $p(r)$ determined by indirect Fourier transformation (Glatter, 1977; Pedersen et al., 1994)
728 and the values are quite close to those from the Guinier fit: $R_g = 53.8 \pm 0.3$ Å and $I(0) = 0.08651 \pm$
729 0.0005 cm^{-1}, where the latter corresponds to a mass of $M = 129$ kDa. The maximum in a normalized
730 Kratky plot using the values of R_g and $I(0)$ from the Guinier fit for normalisation agrees with a
731 relatively compact structure, however, the plateau behaviour for $qR_g > 3$ suggest some openness and
732 potential flexibility of the structure of the complexes. The scattering of the complex from the crystal
733 structure was directly compared to the SAXS data and a poor agreement was observed. To improve
734 the agreement, rigid body refinement (RBR) of the structure was performed using previously
735 described methods (Steiner et al., 2018). For the RBR of HipBST in three connected domains, the

first runs showed that there was some degree of oligomerisation present in the sample, since the model curve is below the measured data at low q. Therefore, a dimer factor $S_{agg}(q) = 1 + \frac{A\sin(qD)}{qD}$ (Larsen et al., 2020) was multiplied with the intensity calculated for the structure. In the expression, A is the mass fraction of dimers of the HipBST complex and D is the distance between the two copies in the dimer. This approach gave good fits to the data.

DATA AND SOFTWARE AVAILABILITY

The accession numbers for the structures reported in this paper are PDB: 7AB3 (HipBST HipT S57A), 7AB4 (HipBST HipT S59A), and 7AB5 (HipBST HipT D233Q).

746 **REFERENCES**

747 Arif, A., Jia, J., Moodt, R. A., DiCorleto, P. E., & Fox, P. L. (2011, Jan 25). Phosphorylation of
748 glutamyl-prolyl tRNA synthetase by cyclin-dependent kinase 5 dictates transcript-selective
749 translational control. *Proceedings of the National Academy of Sciences of the U S A, 108*(4),
750 1415-1420. https://doi.org/10.1073/pnas.1011275108

751 Baugh, L., Phan, I., Begley, D. W., Clifton, M. C., Armour, B., Dranow, D. M., Taylor, B. M.,
752 Muruthi, M. M., Abendroth, J., Fairman, J. W., Fox, D., 3rd, Dieterich, S. H., Staker, B. L.,
753 Gardberg, A. S., Choi, R., Hewitt, S. N., Napuli, A. J., Myers, J., Barrett, L. K., Zhang, Y.,
754 Ferrell, M., Mundt, E., Thompkins, K., Tran, N., Lyons-Abbott, S., Abramov, A., Sekar, A.,
755 Serbzhinskiy, D., Lorimer, D., Buchko, G. W., Stacy, R., Stewart, L. J., Edwards, T. E., Van
756 Voorhis, W. C., & Myler, P. J. (2015, Mar). Increasing the structural coverage of
757 tuberculosis drug targets. *Tuberculosis (Edinb), 95*(2), 142-148.
758 https://doi.org/10.1016/j.tube.2014.12.003

759 Bordes, P., Sala, A. J., Ayala, S., Texier, P., Slama, N., Cirinesi, A. M., Guillet, V., Mourey, L., &
760 Genevaux, P. (2016, Nov 9). Chaperone addiction of toxin-antitoxin systems. *Nat Commun,*
761 *7*, 13339. https://doi.org/10.1038/ncomms13339

762 Brennan, R. G., & Matthews, B. W. (1989, Feb 5). The helix-turn-helix DNA binding motif.
763 *Journal of Biological Chemistry, 264*(4), 1903-1906.
764 https://www.ncbi.nlm.nih.gov/pubmed/2644244

765 Emsley, P., Lohkamp, B., Scott, W. G., & Cowtan, K. (2010, Apr). Features and development of
766 Coot. *Acta Crystallogr D Biol Crystallogr, 66*(Pt 4), 486-501.
767 https://doi.org/10.1107/S0907444910007493

768 Eriani, G., Delarue, M., Poch, O., Gangloff, J., & Moras, D. (1990, Sep 13). Partition of tRNA
769 synthetases into two classes based on mutually exclusive sets of sequence motifs. *Nature,*
770 *347*(6289), 203-206. https://doi.org/10.1038/347203a0

771 Evans, P. (2006, Jan). Scaling and assessment of data quality. *Acta Crystallogr D Biol Crystallogr,*
772 *62*(Pt 1), 72-82. https://doi.org/10.1107/S0907444905036693

773 Evdokimov, A., Voznesensky, I., Fennell, K., Anderson, M., Smith, J. F., & Fisher, D. A. (2009,
774 Aug). New kinase regulation mechanism found in HipBA: a bacterial persistence switch.
775 *Acta Crystallogr D Biol Crystallogr, 65*(Pt 8), 875-879.
776 https://doi.org/10.1107/S0907444909018800

777 Gerdes, K., Baerentsen, R., & Brodersen, D. E. (2021, Jun 29). Phylogeny Reveals Novel HipA-
778 Homologous Kinase Families and Toxin-Antitoxin Gene Organizations. *MBio, 12*(3),
779 e0105821. https://doi.org/10.1128/mBio.01058-21

780 Germain, E., Castro-Roa, D., Zenkin, N., & Gerdes, K. (2013, Oct 24). Molecular mechanism of
781 bacterial persistence by HipA. *Molecular Cell, 52*(2), 248-254.
782 https://doi.org/10.1016/j.molcel.2013.08.045

783 Glatter, O. (1977). New Method for Evaluation of Small-Angle Scattering Data. *Journal of Applied*
784 *Crystallography, 10*(Oct1), 415-421. https://doi.org/Doi 10.1107/S0021889877013879

785 Grabe, G. J., Giorgio, R. T., Hall, A. M. J., Morgan, R. M. L., Dubois, L., Sisley, T. A., Rycroft, J.
786 A., Hare, S. A., & Helaine, S. (2021, Dec). Auxiliary interfaces support the evolution of
787 specific toxin-antitoxin pairing. *Nature Chemical Biology, 17*(12), 1296-1304.
788 https://doi.org/10.1038/s41589-021-00862-y

789 Hallez, R., Geeraerts, D., Sterckx, Y., Mine, N., Loris, R., & Van Melderen, L. (2010, May). New
790 toxins homologous to ParE belonging to three-component toxin-antitoxin systems in
791 Escherichia coli O157:H7. *Molecular Microbiology, 76*(3), 719-732.
792 https://doi.org/10.1111/j.1365-2958.2010.07129.x

793 Hanks, S. K., Quinn, A. M., & Hunter, T. (1988, Jul 1). The protein kinase family: conserved
794 features and deduced phylogeny of the catalytic domains. *Science, 241*(4861), 42-52.
795 https://doi.org/10.1126/science.3291115

796 Harms, A., Brodersen, D. E., Mitarai, N., & Gerdes, K. (2018, Jun 7). Toxins, Targets, and
797 Triggers: An Overview of Toxin-Antitoxin Biology. *Molecular Cell, 70*(5), 768-784.
798 https://doi.org/10.1016/j.molcel.2018.01.003

799 Haseltine, W. A., & Block, R. (1973, May). Synthesis of guanosine tetra- and pentaphosphate
800 requires the presence of a codon-specific, uncharged transfer ribonucleic acid in the acceptor

site of ribosomes. *Proceedings of the National Academy of Sciences of the U S A, 70*(5), 1564-1568. https://doi.org/10.1073/pnas.70.5.1564

Huse, M., & Kuriyan, J. (2002, May 3). The conformational plasticity of protein kinases. *Cell, 109*(3), 275-282. https://doi.org/10.1016/s0092-8674(02)00741-9

Kabsch, W. (2010, Feb). Xds. *Acta Crystallogr D Biol Crystallogr, 66*(Pt 2), 125-132. https://doi.org/10.1107/S0907444909047337

Karplus, P. A., & Diederichs, K. (2012, May 25). Linking crystallographic model and data quality. *Science, 336*(6084), 1030-1033. https://doi.org/10.1126/science.1218231

Krissinel, E., & Henrick, K. (2007, Sep 21). Inference of macromolecular assemblies from crystalline state. *Journal of Molecular Biology, 372*(3), 774-797. https://doi.org/10.1016/j.jmb.2007.05.022

Larsen, A. H., Pedersen, J. S., & Arleth, L. (2020, Aug). Assessment of structure factors for analysis of small-angle scattering data from desired or undesired aggregates. *Journal of Applied Crystallography, 53*(4), 991-1005. https://doi.org/10.1107/S1600576720006500

Letunic, I., & Bork, P. (2019, Jul 2). Interactive Tree Of Life (iTOL) v4: recent updates and new developments. *Nucleic Acids Research, 47*(W1), W256-W259. https://doi.org/10.1093/nar/gkz239

Lim, S., & Kaldis, P. (2013, Aug). Cdks, cyclins and CKIs: roles beyond cell cycle regulation. *Development, 140*(15), 3079-3093. https://doi.org/10.1242/dev.091744

Lyngsø, J., & Pedersen, J. S. (2021). A high-flux automated laboratory small-angle X-ray scattering instrument optimized for solution scattering. *Journal of Applied Crystallography, 54*(1), 295-305. https://doi.org/10.1107/s1600576720016209

McCoy, A. J., Grosse-Kunstleve, R. W., Adams, P. D., Winn, M. D., Storoni, L. C., & Read, R. J. (2007, Aug 1). Phaser crystallographic software. *J Appl Crystallogr, 40*(Pt 4), 658-674. https://doi.org/10.1107/S0021889807021206

826 Minh, B. Q., Schmidt, H. A., Chernomor, O., Schrempf, D., Woodhams, M. D., von Haeseler, A., &
827 Lanfear, R. (2020, May 1). IQ-TREE 2: New Models and Efficient Methods for
828 Phylogenetic Inference in the Genomic Era. *Molecular Biology and Evolution, 37*(5), 1530-
829 1534. https://doi.org/10.1093/molbev/msaa015

830 Pacios, O., Blasco, L., Bleriot, I., Fernandez-Garcia, L., Ambroa, A., Lopez, M., Bou, G., Canton,
831 R., Garcia-Contreras, R., Wood, T. K., & Tomas, M. (2020, Sep 21). (p)ppGpp and Its Role
832 in Bacterial Persistence: New Challenges. *Antimicrobial Agents & Chemotherapy, 64*(10).
833 https://doi.org/10.1128/AAC.01283-20

834 Pedersen, J. S., Hansen, S., & Bauer, R. (1994). The aggregation behavior of zinc-free insulin
835 studied by small-angle neutron scattering. *European Biophysics Journal, 22*(6), 379-389.
836 https://doi.org/10.1007/BF00180159

837 Pereira, S. F., Goss, L., & Dworkin, J. (2011, Mar). Eukaryote-like serine/threonine kinases and
838 phosphatases in bacteria. *Microbiology and Molecular Biology Reviews, 75*(1), 192-212.
839 https://doi.org/10.1128/MMBR.00042-10

840 Schumacher, M. A., Balani, P., Min, J., Chinnam, N. B., Hansen, S., Vulic, M., Lewis, K., &
841 Brennan, R. G. (2015, Aug 6). HipBA-promoter structures reveal the basis of heritable
842 multidrug tolerance. *Nature, 524*(7563), 59-64. https://doi.org/10.1038/nature14662

843 Schumacher, M. A., Min, J., Link, T. M., Guan, Z., Xu, W., Ahn, Y. H., Soderblom, E. J., Kurie, J.
844 M., Evdokimov, A., Moseley, M. A., Lewis, K., & Brennan, R. G. (2012, Sep 27). Role of
845 unusual P loop ejection and autophosphorylation in HipA-mediated persistence and
846 multidrug tolerance. *Cell Rep, 2*(3), 518-525. https://doi.org/10.1016/j.celrep.2012.08.013

847 Schumacher, M. A., Piro, K. M., Xu, W., Hansen, S., Lewis, K., & Brennan, R. G. (2009, Jan 16).
848 Molecular mechanisms of HipA-mediated multidrug tolerance and its neutralization by
849 HipB. *Science, 323*(5912), 396-401. https://doi.org/10.1126/science.1163806

850 Sekine, S., Nureki, O., Dubois, D. Y., Bernier, S., Chenevert, R., Lapointe, J., Vassylyev, D. G., &
851 Yokoyama, S. (2003, Feb 3). ATP binding by glutamyl-tRNA synthetase is switched to the
852 productive mode by tRNA binding. *EMBO Journal, 22*(3), 676-688.
853 https://doi.org/10.1093/emboj/cdg053

854 Sharrock, A., Ruthe, A., Andrews, E. S. V., Arcus, V. A., & Hicks, J. L. (2018). VapC proteins
855 from Mycobacterium tuberculosis share ribonuclease sequence specificity but differ in
856 regulation and toxicity. *PLoS One, 13*(8), e0203412.
857 https://doi.org/10.1371/journal.pone.0203412

858 Sievers, F., & Higgins, D. G. (2018, Jan). Clustal Omega for making accurate alignments of many
859 protein sequences. *Protein Science, 27*(1), 135-145. https://doi.org/10.1002/pro.3290

860 Smart, O. S., Womack, T. O., Flensburg, C., Keller, P., Paciorek, W., Sharff, A., Vonrhein, C., &
861 Bricogne, G. (2012, Apr). Exploiting structure similarity in refinement: automated NCS and
862 target-structure restraints in BUSTER. *Acta Crystallogr D Biol Crystallogr, 68*(Pt 4), 368-
863 380. https://doi.org/10.1107/S0907444911056058

864 Stancik, I. A., Sestak, M. S., Ji, B., Axelson-Fisk, M., Franjevic, D., Jers, C., Domazet-Loso, T., &
865 Mijakovic, I. (2018, Jan 5). Serine/Threonine Protein Kinases from Bacteria, Archaea and
866 Eukarya Share a Common Evolutionary Origin Deeply Rooted in the Tree of Life. *Journal*
867 *of Molecular Biology, 430*(1), 27-32. https://doi.org/10.1016/j.jmb.2017.11.004

868 Steiner, E. M., Lyngso, J., Guy, J. E., Bourenkov, G., Lindqvist, Y., Schneider, T. R., Pedersen, J.
869 S., Schneider, G., & Schnell, R. (2018, Sep). The structure of the N-terminal module of the
870 cell wall hydrolase RipA and its role in regulating catalytic activity. *Proteins, 86*(9), 912-
871 923. https://doi.org/10.1002/prot.25523

872 Taylor, S. S., & Kornev, A. P. (2011, Feb). Protein kinases: evolution of dynamic regulatory
873 proteins. *Trends in Biochemical Sciences, 36*(2), 65-77.
874 https://doi.org/10.1016/j.tibs.2010.09.006

875 Vang Nielsen, S., Turnbull, K. J., Roghanian, M., Baerentsen, R., Semanjski, M., Brodersen, D. E.,
876 Macek, B., & Gerdes, K. (2019, Jun 18). Serine-Threonine Kinases Encoded by Split hipA
877 Homologs Inhibit Tryptophanyl-tRNA Synthetase. *MBio, 10*(3).
878 https://doi.org/10.1128/mBio.01138-19

879 Waterhouse, A. M., Procter, J. B., Martin, D. M., Clamp, M., & Barton, G. J. (2009, May 1).
880 Jalview Version 2--a multiple sequence alignment editor and analysis workbench.
881 *Bioinformatics, 25*(9), 1189-1191. https://doi.org/10.1093/bioinformatics/btp033

882 Wen, Y., Behiels, E., Felix, J., Elegheert, J., Vergauwen, B., Devreese, B., & Savvides, S. N. (2014,
883 Sep). The bacterial antitoxin HipB establishes a ternary complex with operator DNA and
884 phosphorylated toxin HipA to regulate bacterial persistence. *Nucleic Acids Research,*
885 *42*(15), 10134-10147. https://doi.org/10.1093/nar/gku665

886 Winn, M. D., Ballard, C. C., Cowtan, K. D., Dodson, E. J., Emsley, P., Evans, P. R., Keegan, R. M.,
887 Krissinel, E. B., Leslie, A. G., McCoy, A., McNicholas, S. J., Murshudov, G. N., Pannu, N.
888 S., Potterton, E. A., Powell, H. R., Read, R. J., Vagin, A., & Wilson, K. S. (2011, Apr).
889 Overview of the CCP4 suite and current developments. *Acta Crystallogr D Biol Crystallogr,*
890 *67*(Pt 4), 235-242. https://doi.org/10.1107/S0907444910045749

891 Winther, K., Tree, J. J., Tollervey, D., & Gerdes, K. (2016, Nov 16). VapCs of Mycobacterium
892 tuberculosis cleave RNAs essential for translation. *Nucleic Acids Research, 44*(20), 9860-
893 9871. https://doi.org/10.1093/nar/gkw781

894 Winther, K. S., Roghanian, M., & Gerdes, K. (2018, Apr 5). Activation of the Stringent Response
895 by Loading of RelA-tRNA Complexes at the Ribosomal A-Site. *Molecular Cell, 70*(1), 95-
896 105 e104. https://doi.org/10.1016/j.molcel.2018.02.033

897 Zielenkiewicz, U., & Ceglowski, P. (2005, Sep). The toxin-antitoxin system of the streptococcal
898 plasmid pSM19035. *Journal of Bacteriology, 187*(17), 6094-6105.
899 https://doi.org/10.1128/JB.187.17.6094-6105.2005

900

TABLE S1. Crystallographic data statistics

	HipBST^{D233Q}	**HipBST^{S57A}**	**HipBST^{S59A}**
Data Collection			
Wavelength (Å)	1.54180	0.97625	1.54180
Resolution range (Å)	49.9 – 2.9 (3.0 – 2.9)*	46.9 – 2.4 (2.49 – 2.40)*	50.4 – 3.34 (3.5 – 3.4)*
Space group	C121	C121	C121
Unit cell dimensions			
a, b, c, (Å)	281.66, 106.47, 57.75	281.68, 106.07, 57.56	285.26, 107.15, 58.45
α, β, γ (°)	90, 90.75, 90	90, 90.65, 90	90, 90.71, 90
Total reflections	74,587 (7,335)	625,868 (25,597)	41,777 (4,068)
Unique reflections	37,716 (3,719)	66,117 (6,503)	22,580 (2,193)
Multiplicity	2.0 (2.0)	9.5 (3.9)	1.9 (1.9)
Completeness (%)	99.8 (99.3)	99.9 (99.4)	87.71 (84.84)
R_{meas} (%)	0.13 (1.105)	0.27 (0.08)	0.17 (1.01)
I/σ(I)	6.62 (0.86)	10.3 (0.72)	7.10 (0.93)
$CC_{1/2}$	0.99 (0.37)	0.99 (0.37)	0.97 (0.43)
Refinement			
Average B-factor (Å^2)	98.5	86.1	119.4
protein	98.9	86.5	119.9
ligands	-	166.7	118.6
solvent	80.0	76.7	78.3
No. of reflections	37,706 (3,719)	66,112 (6,504)	22,570 (2,193)
No. of reflections (free)	1,914 (175)	3,364 (326)	1086 (86)
R-work (%)	19.5 (31.8)	21.0 (42.8)	20.2 (29.2)
R-free (%)	22.8 (34.5)	23.8 (46.2)	24.3 (35.4)
Number of			
protein (residues)	1,018	1,017	1,023
solvent (atoms)	203	402	110
ligand (atoms)	-	20	10
rmsd (bonds, Å)	0.011	0.013	0.013
rmsd (angles, degrees)	1.49	1.75	1.66
Rotamer outliers (%)	9.8	6.0	10.07
Clashscore	4.4	2.7	5.8
Ramachandran statistics			
favoured (%)	95.1	96.0	95.6
allowed (%)	4.7	3.6	3.9
outliers (%)	0.2	0.4	0.5
Rama-Z score			
whole	-1.63	-0.44	-0.90
helix	-1.27	-0.40	-0.48
sheet	-1.36	0.21	0.07
loop	-0.75	-0.16	-0.73

*Numbers in parentheses refer to the outermost resolution shell.

TABLE S2. Bacterial strains and plasmids.

***E. coli* strains**	**Description**	**Reference or source**
MG1655	Wild-type K12	(Blattner et al., 1997)
O127	O127:H6 strain E2348/69	(Iguchi et al., 2009)
TB28	MG1655Δ*lacIZYA*	Laboratory collection
Plasmid	**Description[a]**	**Reference or source**
pBAD33	p15 *araC* P_{BAD}, Cm^r	(Guzman et al., 1995)
pBAD322T	pMB1 *rop araC* P_{BAD}, Tet^r	(Cronan, 2006)
pNDM220	Mini-R1 $lacI^q$ $P_{A1/04/03}$, Amp^r	(Gotfredsen & Gerdes, 1998)
pGH254	Mini-R1, *lacZYA* transcriptional fusion vector, Kan^r	Laboratory collection
pET-15b	pBR322 *lacI* P_{T7}, Amp^r	Novagen
pKG127	pUC57::$hipBST_{O127}$	(Vang Nielsen et al., 2019)
pSVN1	pBAD33::*hipT*, start codon GTG	(Vang Nielsen et al., 2019)
pSVN68	pUC57::$hipB\text{-}S\text{-}T^{S57A}{}_{His6}$, optimized SDs for all genes	This work
pSVN78	pET-15b::$hipB\text{-}S\text{-}T^{S57A}{}_{His6}$, optimized SDs for all genes	This work
pSVN87	pUC57::$hipB\text{-}S\text{-}T^{D210Q}{}_{His6}$, optimized SDs for all genes	This work

pSVN88	pUC57::*hipB-S-T*^{D233Q}$_{His6}$, optimized SDs for all genes	This work
pSVN96	pET-15b::*hipB-S-T*^{D233Q}$_{His6}$, optimized SDs for all genes	This work
pSVN109	pNDM220::*hipS*, optimized SD	(Vang Nielsen et al., 2019)
pSVN110	pNDM220::*hipB-S*, optimized SDs for both genes	(Vang Nielsen et al., 2019)
pSVN111	pNDM220::*hipB*, optimized SD	(Vang Nielsen et al., 2019)
pSVN141	pGH254::P_{hipBST}-*hipB'-laZ*, transcriptional P_{hipBST}-*hipB' lacZ* fusion	This work
pSVN154	pBAD322T:: *hipB-S-T*^{D210Q}, optimized SDs for all genes	This work
pSVN178	pNDM220::*hipS*^{W65A}, optimized SD	This work
pSVN180	pBAD33::*hipB-S-T*^{D210Q}, optimized SDs for all genes	This work
pSVN181	pBAD33::*hipB-S-T*^{D233Q}, optimized SDs for all genes	This work
pSVN182	pBAD33::*hipB-S*, optimized SDs for both genes	This work
pSVN184	pBAD33::*hipB-T*^{D210Q}, optimized SDs for both genes	This work
pSVN185	pBAD33::*hipB-T*^{D233Q}, optimized SDs for both genes	This work
pSVN187	pBAD33::*hipS-T*^{D210Q}, optimized SDs for both genes	This work
pSVN188	pBAD33::*hipS-T*^{D233Q}, optimized SDs for both genes	This work
pSVN189	pBAD33::*hipB*, optimized SD	This work
pSVN190	pBAD33::*hipS*, optimized SD	This work

pSVN192	pBAD33::*hipT*^{D210Q}, optimized SD	This work
pSVN193	pBAD33::*hipT*^{D233Q}, optimized SD	This work
pSVN194	pBAD33::*hipT*^{S57D}, start codon GTG	This work
pSVN195	pBAD33::*hipT*^{S59D}, start codon GTG	This work
pSVN198	pGH254:: P_{hipBST}-*hipBST-lacZ*, transcriptional P_{hipBST}-*hipBST lacZ* fusion	This work
pSVN199	pBAD33::*hipT*^{S57A}, start codon GTG	This work
pSVN201	pBAD33::*hipT*^{S59A}, start codon GTG	This work
pSVN203	pBAD33::*hipT*$^{S57A+S59A}$, start codon GTG	This work
pSVN205	pBAD33::*hipT*$^{S57D+S59A}$, start codon GTG	This work
pSVN207	pBAD33::*hipT*$^{S57A+S59D}$, start codon GTG	This work
pSVN209	pBAD33::*hipT*$^{S57D+S59D}$, start codon GTG	This work
pSVN211	pBAD33::*hipT*^{D210Q}, start codon GTG	This work
pSVN212	pBAD33::*hipT*$^{S57D+D210Q}$, start codon GTG	This work
pSVN213	pBAD33::*hipT*$^{S59D+D210Q}$, start codon GTG	This work
pSVN214	pBAD33::*hipT*$^{S57A+D210Q}$, start codon GTG	This work
pSVN215	pBAD33::*hipT*$^{S59A+D210Q}$, start codon GTG	This work
pSVN216	pBAD33::*hipT*$^{S57A+S59A+D210Q}$, start codon GTG	This work

pSVN217	pBAD33::*hipT*$^{S57D+S59A+D210Q}$, start codon GTG	This work
pSVN218	pBAD33::*hipT*$^{S57A+S59D+D210Q}$, start codon GTG	This work
pSVN219	pBAD33::*hipT*$^{S57D+S59D+D210Q}$, start codon GTG	This work
pSVN220	pBAD33::*hipT*^{D210Q}, optimized SD	This work
pSVN221	pBAD33::*hipT*$^{S57D+D210Q}$, optimized SD	This work
pSVN222	pBAD33::*hipT*$^{S59D+D210Q}$, optimized SD	This work
pSVN223	pBAD33::*hipT*$^{S57A+D210Q}$, optimized SD	This work
pSVN224	pBAD33::*hipT*$^{S59A+D210Q}$, optimized SD	This work
pSVN225	pBAD33::*hipT*$^{S57A+S59A+D210Q}$, optimized SD	This work
pSVN226	pBAD33::*hipT*$^{S57D+S59A+D210Q}$, optimized SD	This work
pSVN227	pBAD33::*hipT*$^{S57A+S59D+D210Q}$, optimized SD	This work
pSVN228	pBAD33::*hipT*$^{S57D+S59D+D210Q}$, optimized SD	This work
pSNN1	pET-15b::*hipT*$^{S57A}{}_{His6}$, optimized SD	This work
pSNN2	pET-15b::*hipT*$^{S57A+D210A}{}_{His6}$, optimized SD	This work
pMME	pET-15b::*hipB-S-T*$^{S59A}{}_{His6}$, optimized SDs for all genes	This work

[a]SD, Shine-Dalgarno sequence.

TABLE S3. Oligonucleotides and primers.

Oligonucleotide	Sequence
FP1(GTG)	CCCCGTCGACGGATCCAAGGAGTTTTATAAGTGGCGAATTGTCGTATTCTG
FP21	GGGGGGTACCGGATCCAAAATAAGGAGGAAAAAAAAATGATCTGCTCAGGACCAC
FP22	CCCCCTCGAGGGATCCAAAATAAGGAGGAAAAAAAAATGCATCGGCGAGTGAAAG
FP43	CCCCGAATTCCTCTCCCGATGAGATCAGC
FP46	GGGGGGTACCGGATCCAAAATAAGGAGGAAAAAAAAATGCATCGGCGAGTGAAAG
FP47	GGGGGGTACCGGATCCAAAATAAGGAGGAAAAAAAAATGGCGAATTGTCGTATTCTG
FP48	GGGGGTCGACCTGCAGAAAATAAGGAGGAAAAAAAAATGGCGAATTGTCGTATTCTG
FP49	CCCCGAATTCCTCTCCCG ATGAGATCAGCTTTC
RP1	CCCCCGCATGCGAATTCGCTCACAGCAGCCCCAGACG
RP11	CCCCCTCGAGAAGCTTTCACAGCAGCCCCAGACG
RP14	GGGGGAATTCAAGCTTTTATTCCTCCCAAGGTAAAATC
RP15	GGGGGAATTCAAGCTTTCACTCGCCGATGCATAG
RP32	CCCCGGATCCTCTGCAACTCCTGGAGTTG
RP35	GTCCTGAGCAGATCATTAAAGAACC

RP37	CGATTGATAAAAGACAAAAACAAGATC
RP38	GTTGGTCGCCGATCGCTTTC
RP42	GGGGGTCGACCTGCAGTCACTCGCCGATGCATAG
RP43	GGGGGGTACCTCACAGCA GCCCCAGACG
hipS W65A Fw	CAGAAGGAGCTCTGCGTCAACGCTA
hipS W65A Rv	TGACGCAGAGCTCCTTCTGGCGC
HipT S57D Fw	GCGTCAACAAAAAGGGATGGATATTTCCGGTT
HipT S57D Rv	GGGCTGGTAACCGGAAATATCCATCCCTTTTT
HipT S59D Fw	GTCAACAAAAAGGGATGAGTATTGACGGTTAC
HipT S59D Rv	TTGGGCTGGTAACCGTCAATACTCATCCCTTT
HipT S59A Fw	GTCAACAAAAAGGGATGAGTATTGCCGGTTAC
HipT S59A Rv	TTGGGCTGGTAACCGGCAATACTCATCCCTTT
HipT S57A + S59A Fw	CGTCAACAAAAAGGGATGGCTATTGCCGGTTAC
HipT S57A + S59A Rv	TTGGGCTGGTAACCGGCAATAGCCATCCCTTTT
HipT S57D + S59A Fw	CGTCAACAAAAAGGGATGGATATTGCCGGTTAC
HipT S57D + S59A Rv	TTGGGCTGGTAACCGGCAATATCCATCCCTTTT

HipT S57A + S59D Fw	CGTCAACAAAAAGGGATGGCTATTGACGGTTAC
HipT S57A + S59D Rv	TTGGGCTGGTAACCGTCAATAGCCATCCCTTTT
HipT S57D + S59D Fw	CGTCAACAAAAAGGGATGGATATTGACGGTTAC
HipT S57D + S59D Rv	TTGGGCTGGTAACCGTCAATATCCATCCCTTTT
hipX S57A Fw	AAGGGATGGCTATTTCCGGTTACCAGCC
hipX S57A Rv	CGGAAATAGCCATCCTTTTTGTTGACG
hipX D210Q Fw	GTAATAACCAGATGCATTTACGAAACTTTGG
hipX D210Q Rv	AAATGCATCTGGTTATTACCCAGCAACCAGG
hipX D233Q Fw	CGGTGTATCAGTTTGTTTCTGTCGCTCCC
hipX D233Q Rv	GAAACAAACTGATACACCGGCGCTAACG
hipBS del Fw	ACGACAATTCGCCATTTTTTTTTCCTCCTTATTTTTCTAGAGGG
hipBS del Rv	TTCCCCTCTAGAAAAATAAGGAGGAAAAAAAAATGGCGAAT
hipT D210A Fw	TAAATGCATCGCGTTATTACCCAGCAACAA
hipT D210A Rv	CTGGGTAATAACGCGATGCATTTACGAAACTTT
hipT S57S59A Fw	GGGATGAGTATTGCCGGTTACCAGCCCAAATTGCAA
hipT S57S59A Rv	GTAACCGGCAATACTCATCCCTTTTTGTTGACGCGG

SUPPLEMENTARY METHODS

Construction of plasmids. Construction of plasmids is summarised below.

pSVN68. The mutation in *hipB-S-T*^{S57A}$_{His6}$ with optimized SDs for all three genes was created using pSVN61 (Vang Nielsen et al., 2019) and primers hipX S57A Fw and hipX S57A Rv in a site-directed plasmid mutagenesis PCR. Eight reactions were carried out at different temperatures with a gradient PCR. The samples were pooled and digested with DpnI to digest the parental plasmid before being transformed into *E. coli* DH5α.

pSVN78. *hipB-S-T*^{S57A}$_{His6}$ with optimized SDs for all three genes was sub-cloned from pSVN68 by digesting with XbaI and XhoI, purifying the DNA fragment and ligating into pET-15b.

pSVN87. The mutation in *hipB-S-T*^{D210Q}$_{His6}$ with optimized SDs for all three genes was created using pSVN61 (Vang Nielsen et al., 2019) and primers hipX D210Q Fw and hipX D210Q Rv in a site-directed plasmid mutagenesis PCR. Eight reactions were carried out at different temperatures with a gradient PCR. The samples were pooled and digested with DpnI to digest the parental plasmid before being transformed into *E. coli* DH5α.

pSVN88. The mutation in *hipB-S-T*^{D233Q}$_{His6}$ with optimized SDs for all three genes was created using pSVN61 (Vang Nielsen et al., 2019) and primers hipX D233Q Fw and hipX D233Q Rv in a site-directed plasmid mutagenesis PCR. Eight reactions were carried out at different temperatures with a gradient PCR. The samples were pooled and digested with DpnI to digest the parental plasmid before being transformed into *E. coli* DH5α.

pSVN96. *hipB-S-T*^{D233Q}$_{His6}$ with optimized SDs for all three genes was sub-cloned from pSVN88 by digesting with XbaI and XhoI, purifying the DNA fragment and ligating into pET-15b.

24 **pSVN141.** P_{hipBST}-*hipB*', a fragment containing 224 bp upstream of the *hipB* gene plus the first
25 73 bp of the *hipB* gene was amplified from pKG127 using primers FP43 and RP32. The
26 resulting PCR product was digested with EcoRI and BamHI and ligated into pGH254.
27 **pSVN154.** *hipB-S-T*^{D210Q} with optimized SDs for all three genes was amplified from pSVN87
28 using primers FP21 and RP11. The resulting PCR product was digested with KpnI and HindIII
29 and ligated into pBAD322T.
30 **pSVN178.** *hipS*^{W65A} was created by a two-step PCR reaction. Two fragments were amplified
31 from pSVN109 using primers FP22 and hipS W65A Rv in one reaction and hipS W65A Fw
32 and RP14 in the other. The resulting two PCR products were joined by a second round of PCR
33 using both fragments as template DNA and primers FP22 and RP14. The final PCR product
34 was digested with XhoI and EcoRI and ligated into pNDM220.
35 **pSVN180.** *hipB-S-T*^{D210Q} with optimized SDs for all three genes was amplified from pSVN87
36 using primers FP21 and RP11. The resulting PCR product was digested with KpnI and HindIII
37 and ligated into pBAD33.
38 **pSVN181.** *hipB-S-T*^{D233Q} with optimized SDs for all three genes was amplified from pSVN88
39 using primers FP21 and RP11. The resulting PCR product was digested with KpnI and HindIII
40 and ligated into pBAD33.
41 **pSVN182.** *hipB-S* with optimized SDs for both genes was amplified from pSVN87 using
42 primers FP21 and RP14. The resulting PCR product was digested with KpnI and HindIII and
43 ligated into pBAD33.
44 **pSVN184.** *hipB-T*^{D210Q} with optimized SDs for both genes was created by amplifying two PCR
45 products from pSVN87: *hipB* using primers FP21 and RP42 and *hipT*^{D210Q} using primers FP48
46 and RP11. The *hipB* fragment was digested with KpnI and PstI, while the *hipT*^{D233Q} fragment
47 was digested with PstI and HindIII. The two digested fragments were then ligated into pBAD33
48 using the KpnI and HindIII restriction sites.

49 **pSVN185.** *hipB-T*^{D233Q} with optimized SDs for both genes was created by amplifying two PCR
50 products from pSVN88: *hipB* using primers FP21 and RP42 and *hipT*^{D233Q} using primers FP48
51 and RP11. The *hipB* fragment was digested with KpnI and PstI, while the *hipT*^{D233Q} fragment
52 was digested with PstI and HindIII. The two digested fragments were then ligated into pBAD33
53 using the KpnI and HindIII restriction sites.
54 **pSVN187.** *hipS-T*^{D210Q} with optimized SDs for both genes was amplified from pSVN88 using
55 primers FP46 and RP11. The resulting PCR product was digested with KpnI and HindIII and
56 ligated into pBAD33.
57 **pSVN188.** *hipS-T*^{D233Q} with optimized SDs for both genes was amplified from pSVN87 using
58 primers FP46 and RP11. The resulting PCR product was digested with KpnI and HindIII and
59 ligated into pBAD33.
60 **pSVN189.** *hipB* with optimized SD was amplified from pSVN87 using primers FP21 and
61 RP15. The resulting PCR product was digested with KpnI and HindIII and ligated into
62 pBAD33.
63 **pSVN190.** *hipS* with optimized SD was amplified from pSVN87 using primers FP46 and
64 RP14. The resulting PCR product was digested with KpnI and HindIII and ligated into
65 pBAD33.
66 **pSVN192.** *hipT*^{D210Q} with optimized SD was amplified from pSVN87 using primers FP47 and
67 RP11. The resulting PCR product was digested with KpnI and HindIII and ligated into
68 pBAD33.
69 **pSVN193.** *hipT*^{D233Q} with optimized SD was amplified from pSVN88 using primers FP47 and
70 RP11. The resulting PCR product was digested with KpnI and HindIII and ligated into
71 pBAD33.
72 **pSVN194.** *hipT*^{S57D} with start codon GTG was created by a two-step PCR reaction. Two
73 fragments were amplified from pKG127 using primers FP1(GTG) and HipT S57D Rv in one

reaction and HipT S57D Fw and RP1 in the other. The resulting two PCR products were joined by a second round of PCR using both fragments as template DNA and primers FP1(GTG) and RP1. The final PCR product was digested with SalI and SphI and ligated into pBAD33.

pSVN195. *hipT*^{S59D} with start codon GTG was created by a two-step PCR reaction. Two fragments were amplified from pKG127 using primers FP1(GTG) and HipT S59D Rv in one reaction and HipT S59D Fw and RP1 in the other. The resulting two PCR products were joined by a second round of PCR using both fragments as template DNA and primers FP1(GTG) and RP1. The final PCR product was digested with SalI and SphI and ligated into pBAD33.

pSVN198. P_{hipBST}-*hipBST*, a fragment containing 224 bp upstream of the *hipB* gene plus the native *hipBST* operon was amplified from pKG127 using primers FP49 and RP43. The resulting PCR product was digested with EcoRI and KpnI and ligated into pGH254.

pSVN199. *hipT*^{S57A} with start codon GTG was amplified from pSVN78 using primers FP1(GTG) and RP1. The resulting PCR product was digested with SalI and SphI and ligated into pBAD33.

pSVN201. *hipT*^{S59A} with start codon GTG was created by a two-step PCR reaction. Two fragments were amplified from pKG127 using primers FP1(GTG) and HipT S59A Rv in one reaction and HipT S59A Fw and RP1 in the other. The resulting two PCR products were joined by a second round of PCR using both fragments as template DNA and primers FP1(GTG) and RP1. The final PCR product was digested with SalI and SphI and ligated into pBAD33.

pSVN203. *hipT*$^{S57A+S59A}$ with start codon GTG was created by a two-step PCR reaction. Two fragments were amplified from pKG127 using primers FP1(GTG) and HipT S57A + S59A Rv in one reaction and HipT S57A + S59A Fw and RP1 in the other. The resulting two PCR products were joined by a second round of PCR using both fragments as template DNA and primers FP1(GTG) and RP1. The final PCR product was digested with SalI and SphI and ligated into pBAD33.

99 **pSVN205.** *hipT*$^{S57D+S59A}$ with start codon GTG was created by a two-step PCR reaction. Two
100 fragments were amplified from pKG127 using primers FP1(GTG) and HipT S57D + S59A Rv
101 in one reaction and HipT S57D + S59A Fw and RP1 in the other. The resulting two PCR
102 products were joined by a second round of PCR using both fragments as template DNA and
103 primers FP1(GTG) and RP1. The final PCR product was digested with SalI and SphI and
104 ligated into pBAD33.
105 **pSVN207.** *hipT*$^{S57A+S59D}$ with start codon GTG was created by a two-step PCR reaction. Two
106 fragments were amplified from pKG127 using primers FP1(GTG) and HipT S57A + S59D Rv
107 in one reaction and HipT S57A + S59D Fw and RP1 in the other. The resulting two PCR
108 products were joined by a second round of PCR using both fragments as template DNA and
109 primers FP1(GTG) and RP1. The final PCR product was digested with SalI and SphI and
110 ligated into pBAD33.
111 **pSVN209.** *hipT*$^{S57D+S59D}$ with start codon GTG was created by a two-step PCR reaction. Two
112 fragments were amplified from pKG127 using primers FP1(GTG) and HipT S57D + S59D Rv
113 in one reaction and HipT S57D + S59D Fw and RP1 in the other. The resulting two PCR
114 products were joined by a second round of PCR using both fragments as template DNA and
115 primers FP1(GTG) and RP1. The final PCR product was digested with SalI and SphI and
116 ligated into pBAD33.
117 **pSVN211.** *hipT*^{D210Q} with start codon GTG was created by a two-step PCR reaction. Two
118 fragments were amplified from pSVN1 using primers FP1(GTG) and hipX D210Q Rv in one
119 reaction and hipX D210Q Fw and RP1 in the other. The resulting two PCR products were
120 joined by a second round of PCR using both fragments as template DNA and primers
121 FP1(GTG) and RP1. The final PCR product was digested with SalI and SphI and ligated into
122 pBAD33.

123 **pSVN212.** *hipT*$^{S57D+D210Q}$ with start codon GTG was created by a two-step PCR reaction. Two
124 fragments were amplified from pSVN194 using primers FP1(GTG) and hipX D210Q Rv in
125 one reaction and hipX D210Q Fw and RP1 in the other. The resulting two PCR products were
126 joined by a second round of PCR using both fragments as template DNA and primers
127 FP1(GTG) and RP1. The final PCR product was digested with SalI and SphI and ligated into
128 pBAD33.
129 **pSVN213.** *hipT*$^{S59D+D210Q}$ with start codon GTG was created by a two-step PCR reaction. Two
130 fragments were amplified from pSVN195 using primers FP1(GTG) and hipX D210Q Rv in
131 one reaction and hipX D210Q Fw and RP1 in the other. The resulting two PCR products were
132 joined by a second round of PCR using both fragments as template DNA and primers
133 FP1(GTG) and RP1. The final PCR product was digested with SalI and SphI and ligated into
134 pBAD33.
135 **pSVN214.** *hipT*$^{S57A+D210Q}$ with start codon GTG was created by a two-step PCR reaction. Two
136 fragments were amplified from pSVN199 using primers FP1(GTG) and hipX D210Q Rv in
137 one reaction and hipX D210Q Fw and RP1 in the other. The resulting two PCR products were
138 joined by a second round of PCR using both fragments as template DNA and primers
139 FP1(GTG) and RP1. The final PCR product was digested with SalI and SphI and ligated into
140 pBAD33.
141 **pSVN215.** *hipT*$^{S59A+D210Q}$ with start codon GTG was created by a two-step PCR reaction. Two
142 fragments were amplified from pSVN201 using primers FP1(GTG) and hipX D210Q Rv in
143 one reaction and hipX D210Q Fw and RP1 in the other. The resulting two PCR products were
144 joined by a second round of PCR using both fragments as template DNA and primers
145 FP1(GTG) and RP1. The final PCR product was digested with SalI and SphI and ligated into
146 pBAD33.

147 **pSVN216.** *hipT*$^{S57A+S59A+D210Q}$ with start codon GTG was created by a two-step PCR reaction.
148 Two fragments were amplified from pSVN203 using primers FP1(GTG) and hipX D210Q Rv
149 in one reaction and hipX D210Q Fw and RP1 in the other. The resulting two PCR products
150 were joined by a second round of PCR using both fragments as template DNA and primers
151 FP1(GTG) and RP1. The final PCR product was digested with SalI and SphI and ligated into
152 pBAD33.
153 **pSVN217.** *hipT*$^{S57D+S59A+D210Q}$ with start codon GTG was created by a two-step PCR reaction.
154 Two fragments were amplified from pSVN205 using primers FP1(GTG) and hipX D210Q Rv
155 in one reaction and hipX D210Q Fw and RP1 in the other. The resulting two PCR products
156 were joined by a second round of PCR using both fragments as template DNA and primers
157 FP1(GTG) and RP1. The final PCR product was digested with SalI and SphI and ligated into
158 pBAD33.
159 **pSVN218.** *hipT*$^{S57A+S59D+D210Q}$ with start codon GTG was created by a two-step PCR reaction.
160 Two fragments were amplified from pSVN207 using primers FP1(GTG) and hipX D210Q Rv
161 in one reaction and hipX D210Q Fw and RP1 in the other. The resulting two PCR products
162 were joined by a second round of PCR using both fragments as template DNA and primers
163 FP1(GTG) and RP1. The final PCR product was digested with SalI and SphI and ligated into
164 pBAD33.
165 **pSVN219.** *hipT*$^{S57D+S59D+D210Q}$ with start codon GTG was created by a two-step PCR reaction.
166 Two fragments were amplified from pSVN209 using primers FP1(GTG) and hipX D210Q Rv
167 in one reaction and hipX D210Q Fw and RP1 in the other. The resulting two PCR products
168 were joined by a second round of PCR using both fragments as template DNA and primers
169 FP1(GTG) and RP1. The final PCR product was digested with SalI and SphI and ligated into
170 pBAD33.

171 **pSVN220.** *hipT*^{D210Q} with optimized SD was amplified from pSVN211 using primers FP48
172 and RP11. The resulting PCR product was digested with PstI and HindIII and ligated into
173 pBAD33.
174 **pSVN221.** *hipT*$^{S57D+D210Q}$ with optimized SD was amplified from pSVN212 using primers
175 FP48 and RP11. The resulting PCR product was digested with PstI and HindIII and ligated into
176 pBAD33.
177 **pSVN222.** *hipT*$^{S59D+D210Q}$ with optimized SD was amplified from pSVN213 using primers
178 FP48 and RP11. The resulting PCR product was digested with PstI and HindIII and ligated into
179 pBAD33.
180 **pSVN223.** *hipT*$^{S57A+D210Q}$ with optimized SD was amplified from pSVN214 using primers
181 FP48 and RP11. The resulting PCR product was digested with PstI and HindIII and ligated into
182 pBAD33.
183 **pSVN224.** *hipT*$^{S59A+D210Q}$ with optimized SD was amplified from pSVN215 using primers
184 FP48 and RP11. The resulting PCR product was digested with PstI and HindIII and ligated into
185 pBAD33.
186 **pSVN225.** *hipT*$^{S57A+S59A+D210Q}$ with optimized SD was amplified from pSVN216 using primers
187 FP48 and RP11. The resulting PCR product was digested with PstI and HindIII and ligated into
188 pBAD33.
189 **pSVN226.** *hipT*$^{S57D+S59A+D210Q}$ with optimized SD was amplified from pSVN217 using primers
190 FP48 and RP11. The resulting PCR product was digested with PstI and HindIII and ligated into
191 pBAD33.
192 **pSVN227.** *hipT*$^{S57A+S59D+D210Q}$ with optimized SD was amplified from pSVN218 using primers
193 FP48 and RP11. The resulting PCR product was digested with PstI and HindIII and ligated into
194 pBAD33.

195 **pSVN228.** *hipT*$^{S57D+S59D+D210Q}$ with optimized SD was amplified from pSVN219 using primers
196 FP48 and RP11. The resulting PCR product was digested with PstI and HindIII and ligated into
197 pBAD33.
198 **pSNN1**. *hipT*^{S57A} with optimized SD was amplified from pSVN78 using primers hipBS del Fw
199 and hipBS del Rv. This resulted in the deletion of HipB and HipS.
200 **pSNN2.** *hipT*$^{S57A+D210A}$ with optimized SD was amplified from pSNN1 using primers hipT
201 D210A Fw and hipT D210A Rv.
202 **pMME3**. *hipBST*^{S59A} with optimized SD was amplified from pSVN78 using primers hipT
203 S57S59A Fw and hipT S57S59A Rv to introduce the mutations A57S and S59A.
204

SUPPLEMENTARY FIGURE LEGENDS

Figure S1. Sequence alignment with consensus structural elements of HipBST, $HipBA_{Ec}$ and $HipBA_{So}$. a. Alignment of *E. coli* O127:H6 HipB with HipB from *E. coli* K-12 HipBA and HipB from *S. oneidensis* HipBA. Secondary structure observed in *E. coli* O127:H6 HipB is shown above the sequences, except for α1*, which is missing from the crystal structures but predicted by JPred4 (Drozdetskiy et al., 2015). **b.** Alignment of *E. coli* O127:H6 HipS with the N-terminal subdomain 1 from *E. coli* K-12 HipA and *S. oneidensis* HipA. The position of the the Gly-rich interacting helix (α3) of HipS is indicated. Secondary structure observed in *E. coli* O127:H6 HipS is shown above the sequences **c.** Alignment of *E. coli* O127:H6 HipT with the main kinase domain of *E. coli* K-12 HipA and *S. oneidensis* HipA. The position of the Gly-rich loop (residue 58-63) and phosphorylation sites (Ser57 and Ser59), catalytic motif (Asp210), and Mg^{2+}-binding motif (Asp233), are indicated. Secondary structure observed in *E. coli* O127:H6 HipT is shown above the sequences.

Figure S2. Biophysical analysis of the HipBST complex. a. Sequence alignment of *E. coli* O127:H6 and selected HipS orthologues with the N-terminal subdomain 1 of *E. coli* K-12 HipA (bottom). Secondary structure as observed for *E. coli* O127:H6 HipS is indicated above the alignment. Fully conserved residues are shown on a dark orange background, partially conserved residues in orange text, and regions that interact with HipT are shown on a light grey background. Trp65 that intercalates in HipT is shown on a blue background. **b.** Size exclusion chromatography profile as observed for $HipBST^{D233Q}$. A similar elution profile was observed for the other HipBST variants used for structural studies. Absorption at 280 (A_{280}, blue) and 260 (A_{260}, red) nm are shown along with elution volumes of a range of standard proteins (6.5-440 kDa, as indicated). **c.** The structure of *S. oneidensis* HipBA (PDB: 4PU3, HipA purple, HipB green) bound to DNA (orange backbone, blue bases) (Wen et al., 2014).

Figure S3. Interactions of HipT with HipS and HipB. a. Overall fold of HipS with secondary structure elements labelled (α helices in red and β sheets in yellow). **b.** Structural comparison between *E. coli* O127:H6 HipB (cartoon, two shades of green) and the corresponding homodimer of *S. oneidensis* HipB (PDB: 4PU3, ribbons, cyan) showing their conserved structure with similar HTH folds (Wen et al., 2014). **c.** Top, structural alignment of the *E. coli* O127:H6 HipBST complex (HipT, blue; HipS, beige; HipB, green) with *S. oneidensis* HipBA bound to DNA (PDB: 4PU3; HipA, purple; HipB, green) (Wen et al., 2014); Below, close-up views of conserved, basic residues on HipA that contact the DNA backbone (left) and the corresponding region in HipT (right). **d.** Growth curves of *E. coli* MG1655 grown in YT medium and harbouring empty pBAD33 vector ("pBAD33") or pSVN1 (pBAD33::*hipT*, "*hipT*"), in combination with empty pNDM220 vector ("pNDM220"), pSVN109 (pNDM220::*hipS*, "*hipS*"), or pSVN178 (pNDM220::*hipS*^{W65A}, "*hipS*^{W65A}") as indicated. At the indicated times, 0.2% arabinose was added to induce *hipT* (long arrow) and 200 μM IPTG was added to induce *hipS* or *hipS*^{W65A} (short arrow). The data points represent mean values of results from at least three independent experiments, and error bars show standard deviations (hidden when small).

Figure S4. HipT autophosphorylation at Ser57 and Ser59 affects function differentially. a. Active site region and Gly-rich loop (ruby) of *E. coli* O127:H6 HipT from the HipBST^{S57A} structure showing the 2mFo-DFc difference electron density covering Ser59, contoured at 1.2 σ. The phosphate group was refined to an occupancy of 0.89. **b.** Similar view from the HipBST^{S59A} structure showing the 2mFo-DFc difference electron density covering Ser57, contoured at 1.0 σ. The phosphate group was refined to an occupancy of 0.72. **c.** Top, structural alignment of the active sites of *E. coli* O127:H6 HipT S57A (blue) with *E. coli* K-12 HipA

255 ($HipA_{Ec}$, purple) highlighting the positions of their respective phosphoserine (P-Ser) residues,
256 as indicated; Bottom, equivalent structural alignment of the active sites of *E. coli* O127:H6
257 HipT S59A (blue) with *S. oneidensis* HipA ($HipA_{So}$, pale blue). **d.** Growth curves of *E. coli*
258 MG1655 strains grown in YT medium and harbouring empty pBAD33 vector, pSVN1
259 (pBAD33::*hipT*, "*hipT* (SIS, *wt*)"), or single autophosphorylation mutants pSVN194
260 (pBAD33::$hipT^{S57D}$, "*hipT* (DIS)"), pSVN195 (pBAD33::$hipT^{S59D}$, "*hipT* (SID)"), pSVN199
261 (pBAD33::$hipT^{S57A}$, "*hipT* (AIS)"), or pSVN201 (pBAD33::$hipT^{S59A}$, "*hipT* (SIA)") in
262 combination with pSVN110 (pNDM220::*hipB-S*, "*hipBS*"). At the indicated times, 0.2%
263 arabinose was added to induce *hipT* (long arrow) and 200 µMwas added to induce *hipBS* (short
264 arrow). The data points represent mean values of results from two independent experiments,
265 and error bars show standard deviations (hidden when small). **e.** As in **d** but for double
266 autophosphorylation mutants pSVN203 (pBAD33::$hipT^{S57A+S59A}$, "*hipT* (AIA)"), pSVN205
267 (pBAD33::$hipT^{S57D+S59A}$, "*hipT* (DIA)"), pSVN207 (pBAD33::$hipT^{S57A+S59D}$, "*hipT* (AID)"),
268 and pSVN209 (pBAD33::$hipT^{S57D+S59D}$, "*hipT* (DID)"). Data points represent mean values of
269 results from two independent experiments, and error bars designate standard deviations. **f.**
270 Northern blot analysis using probe directed against $tRNA^{gltTUVW}$ (top) and $tRNA^{argVYZQ}$
271 (bottom) based on RNA extracted from *E. coli* MG1655 harbouring pSVN110
272 (pNDM220::*hipB-S*) in combination with pSVN1 (pBAD33::*hipT*, "*hipT* ($S^{57}IS^{59}$, *wt*)"),
273 pSVN194 (pBAD33::$hipT^{S57D}$, "*hipT* ($D^{57}IS^{59}$)"), pSVN195 (pBAD33::$hipT^{S59D}$, "*hipT*
274 ($S^{57}ID^{59}$)"), pSVN209 (pBAD33::$hipT^{S57D+S59D}$, "*hipT* ($D^{57}ID^{59}$)") or pSVN205
275 (pBAD33::$hipT^{S57D+S59A}$, "*hipT* ($D^{57}IA^{59}$)") at indicated time points in minutes before (-) and
276 after (+) addition of 0.2% arabinose to induce wildtype *hipT* or autophosphorylation mutants.
277 Results from strains harbouring pSVN1 (pBAD33::*hipT*), pSVN194 (pBAD33::$hipT^{S57D}$),
278 pSVN209 and (pBAD33::$hipT^{S57D+S59D}$) are representative of two independent experiments,

whereas results from strains harbouring pSVN195 (pBAD33::*hipT*^{S59D}) and pSVN205 (pBAD33::*hipT*$^{S57D+S59A}$) are from single experiments.

Figure S5. Transcriptional regulation of the HipBST system of *E. coli* O127:H6. a. Transcriptional reporter assay using a plasmid with the *hipBST* promoter region and a 5' fragment of the *hipB* gene (including 224 bp upstream of *hipB* plus the first 73 bp of the *hipB* gene, shown with a lightening symbol) transcriptionally fused to *lacZ*. *E. coli* TB28 harbouring the reporter plasmid (pSVN141, pGH254::P$_{hipBST}$-*hipB*'-*lacZ*) and empty pBAD33 vector or combinations of *hipB*, *hipS*, and *hipT* in the context of the HipT^{D233Q} inactive mutant; pSVN180 (pBAD33::*hipB-S-T*^{D233Q}, "*hipBST*^{D233Q}"), pSVN182 (pBAD33::*hipB-S*, "*hipBS*"), pSVN184 (pBAD33::*hipB-T*^{D233Q}, "*hipBT*^{D233Q}"), pSVN187 (pBAD33::*hipS-T*^{D233Q}, "*hipST*^{D233Q}"), pSVN189 (pBAD33::*hipB*, "*hipB*"), pSVN190 (pBAD33::*hipS*, "*hipS*"), or pSVN192 (pBAD33::*hipT*^{D233Q}, "*hipT*^{D233Q}") were grown, diluted, and spotted onto YT agar plates containing 40 µg/ml X-gal and 0.2% glucose (to repress *hipB*/*S*/*T*^{D233Q}) or 0.2% arabinose (to induce *hipB*/*S*/*T*^{D233Q}). Results are representative of two independent experiments. **b.** Overexpression of inactive HipT^{D210Q} and HipT^{D233Q} increases the level of active wildtype HipT from the *hipBST* operon transcriptionally fused to *lacZ* in *E. coli* TB28. The strain harbouring empty pGH254 vector or pSVN198 (pGH254::P$_{hipBST}$-*hipBST-lacZ*, "*hipBST*") in combination with the empty pBAD33 vector, pSVN192 (pBAD33::*hipT*^{D210Q}, "*hipT*^{D210Q}"), or pSVN193 (pBAD33::*hipT*^{D233Q}, "*hipT*^{D233Q}"), as indicated, were grown, diluted, and spotted onto YT agar plates containing 40 µg/ml X-gal without 0.2% arabinose (to obtain only a leaky expression of *hipT*$^{D210Q/D233Q}$), or with 0.2% arabinose (to induce *hipT*$^{D210Q/D233Q}$). Results are from a single experiment. **c.** Primer extension analysis mapping the transcriptional start site in *E. coli* TB28 harbouring pSVN141 (pGH254::P$_{hipBST}$-*hipB*'-*lacZ*), in combination with the empty pBAD322T vector, or pSVN154 (pBAD322T::*hipB-S-T*^{D210Q}), as indicated were grown

and harvested at OD_{600}≈0.4. **d.** Primer extension analysis mapping the transcriptional start site in *E. coli* O127:H6 harbouring pSVN192 (pBAD33::*hipT*^{D210Q}). At OD_{600}≈0.4, 0.2% arabinose was added (to induce *hipT*^{D210Q}), samples were taken at indicated time points and primer extension performed. **e.** The *hipBST* promoter region showing the transcriptional start site (arrow) and corresponding -10 and -35 sequences (red). The start codon of the *hipB* gene ("Met") and putative Shine-Dalgarno sequence ("SD") are indicated as well. **f.** Spot assays using *E. coli* MG1655 harbouring pSVN111 (pNDM220::*hipB*) in combination with the empty pBAD33 vector, pSVN211 (pBAD33::*hipT*^{D210Q}, "*hipT* ($S^{57}IS^{59}$, *wt*)"), pSVN212 (pBAD33::*hipT*$^{S57D+D210Q}$, "*hipT* ($D^{57}IS^{59}$)"), pSVN213 (pBAD33::*hipT*$^{S59D+D210Q}$, "*hipT* ($S^{57}ID^{59}$)"), pSVN214 (pBAD33::*hipT*$^{S57A+D210Q}$, "*hipT* ($A^{57}IS^{59}$)"), pSVN215 (pBAD33::*hipT*$^{S59A+D210Q}$, "*hipT* ($S^{57}IA^{59}$)"), pSVN216 (pBAD33::*hipT*$^{S57A+S59A+D210Q}$, "*hipT* ($A^{57}IA^{59}$)"), pSVN217 (pBAD33::*hipT*$^{S57D+S59A+D210Q}$, "*hipT* ($D^{57}IA^{59}$)"), pSVN218 (pBAD33::*hipT*$^{S57A+S59D+D210Q}$, "*hipT* ($A^{57}ID^{59}$)"), or pSVN219 (pBAD33::*hipT*$^{S57D+S59D+D210Q}$, "*hipT* ($D^{57}ID^{59}$)") spotted onto YT agar plates containing 0.2% glucose (to repress *hipT*^{D210Q} autophosphorylation mutants), 0.2% arabinose (to induce *hipT*^{D210Q} autophosphorylation mutants) or 0.2% arabinose plus 500 μM IPTG (to induce *hipB*). Results are from a single experiment.

Figure S6. Analysis of HipBST using small-angle x-ray scattering. a. Background-subtracted and normalized SAXS data measured for HipBST^{S57A} with indirect Fourier transform fit. **b.** Guinier plot. **c.** *p*(r) from indirect Fourier transform. **d.** Normalized Kratky plot using *I*(0) and R_g from the Guinier fit.

Figure S7. HipT is structurally similar to eukaryotic cyclin-dependent kinases (Cdks). a. Domain overview (top) and secondary structure comparison (bottom) between *E. coli* O127:H6

329 HipT and human CDK5 showing the unique N-terminal mini-domain found in HipT (dashed)
330 and that the N-terminal subdomain 2 is similar to the N-terminal lobe of CDK5 while the core
331 kinase domain is similar to the C-terminal lobe. Conserved features and active site residues are
332 marked with numbers and listed below. **b.** Structural comparison of *E. coli* O127:H6 HipT
333 (top) and human CDK5 (PDB: 4AU8, bottom) (Malmstrom et al., 2012) shown in rainbow
334 colours from N (blue) to C (red) terminus. α-helices are shown as cylinders and for CDK5
335 named in accordance with classical Cdk nomenclature. The two proteins differ in tertiary fold
336 despite similar topology. **c.** Top, overview structure of Human CDK9 (salmon, PDB: 3BLT)
337 with the C-spine region shown as surface (cyan) (Baumli et al., 2008); below, details of the
338 active site bound to ATP with relevant residues indicated. **d.** Top, overview of the *E. coli*
339 O127:H6 HipT structure with the C/R spine region shown as surface (green); below, details of
340 the active site. **e.** Top, overview of the *E. coli* K-12 HipA structure (PDB: 3DNT) with the C/R
341 spine region shown as surface (orange) (Schumacher et al., 2009); below, details of the active
342 site bound to ATP.
343

REFERENCES

Baumli, S., Lolli, G., Lowe, E. D., Troiani, S., Rusconi, L., Bullock, A. N., Debreczeni, J. E., Knapp, S., & Johnson, L. N. (2008, Jul 9). The structure of P-TEFb (CDK9/cyclin T1), its complex with flavopiridol and regulation by phosphorylation. *EMBO Journal, 27*(13), 1907-1918. https://doi.org/10.1038/emboj.2008.121

Blattner, F. R., Plunkett, G., 3rd, Bloch, C. A., Perna, N. T., Burland, V., Riley, M., Collado-Vides, J., Glasner, J. D., Rode, C. K., Mayhew, G. F., Gregor, J., Davis, N. W., Kirkpatrick, H. A., Goeden, M. A., Rose, D. J., Mau, B., & Shao, Y. (1997, Sep 5). The complete genome sequence of Escherichia coli K-12. *Science, 277*(5331), 1453-1462. https://doi.org/10.1126/science.277.5331.1453

Cronan, J. E. (2006, Mar). A family of arabinose-inducible Escherichia coli expression vectors having pBR322 copy control. *Plasmid, 55*(2), 152-157. https://doi.org/10.1016/j.plasmid.2005.07.001

Drozdetskiy, A., Cole, C., Procter, J., & Barton, G. J. (2015, Jul 1). JPred4: a protein secondary structure prediction server. *Nucleic Acids Research, 43*(W1), W389-394. https://doi.org/10.1093/nar/gkv332

Gotfredsen, M., & Gerdes, K. (1998, Aug). The Escherichia coli relBE genes belong to a new toxin-antitoxin gene family. *Molecular Microbiology, 29*(4), 1065-1076. https://doi.org/10.1046/j.1365-2958.1998.00993.x

Guzman, L. M., Belin, D., Carson, M. J., & Beckwith, J. (1995, Jul). Tight regulation, modulation, and high-level expression by vectors containing the arabinose PBAD promoter. *Journal of Bacteriology, 177*(14), 4121-4130. https://doi.org/10.1128/jb.177.14.4121-4130.1995

Iguchi, A., Thomson, N. R., Ogura, Y., Saunders, D., Ooka, T., Henderson, I. R., Harris, D., Asadulghani, M., Kurokawa, K., Dean, P., Kenny, B., Quail, M. A., Thurston, S., Dougan, G., Hayashi, T., Parkhill, J., & Frankel, G. (2009, Jan). Complete genome sequence and comparative genome analysis of enteropathogenic *Escherichia coli* O127:H6 strain E2348/69. *Journal of Bacteriology, 191*(1), 347-354. https://doi.org/10.1128/JB.01238-08

373 Malmstrom, J., Viklund, J., Slivo, C., Costa, A., Maudet, M., Sandelin, C., Hiller, G., Olsson,
374 L. L., Aagaard, A., Geschwindner, S., Xue, Y., & Vasange, M. (2012, Sep 15).
375 Synthesis and structure-activity relationship of 4-(1,3-benzothiazol-2-yl)-thiophene-2-
376 sulfonamides as cyclin-dependent kinase 5 (cdk5)/p25 inhibitors. *Bioorganic and*
377 *Medicinal Chemistry Letters, 22*(18), 5919-5923.
378 https://doi.org/10.1016/j.bmcl.2012.07.068

379 Schumacher, M. A., Piro, K. M., Xu, W., Hansen, S., Lewis, K., & Brennan, R. G. (2009, Jan
380 16). Molecular mechanisms of HipA-mediated multidrug tolerance and its
381 neutralization by HipB. *Science, 323*(5912), 396-401.
382 https://doi.org/10.1126/science.1163806

383 Vang Nielsen, S., Turnbull, K. J., Roghanian, M., Baerentsen, R., Semanjski, M., Brodersen,
384 D. E., Macek, B., & Gerdes, K. (2019, Jun 18). Serine-Threonine Kinases Encoded by
385 Split hipA Homologs Inhibit Tryptophanyl-tRNA Synthetase. *MBio, 10*(3).
386 https://doi.org/10.1128/mBio.01138-19

387 Wen, Y., Behiels, E., Felix, J., Elegheert, J., Vergauwen, B., Devreese, B., & Savvides, S. N.
388 (2014, Sep). The bacterial antitoxin HipB establishes a ternary complex with operator
389 DNA and phosphorylated toxin HipA to regulate bacterial persistence. *Nucleic Acids*
390 *Research, 42*(15), 10134-10147. https://doi.org/10.1093/nar/gku665
391

Figure S1

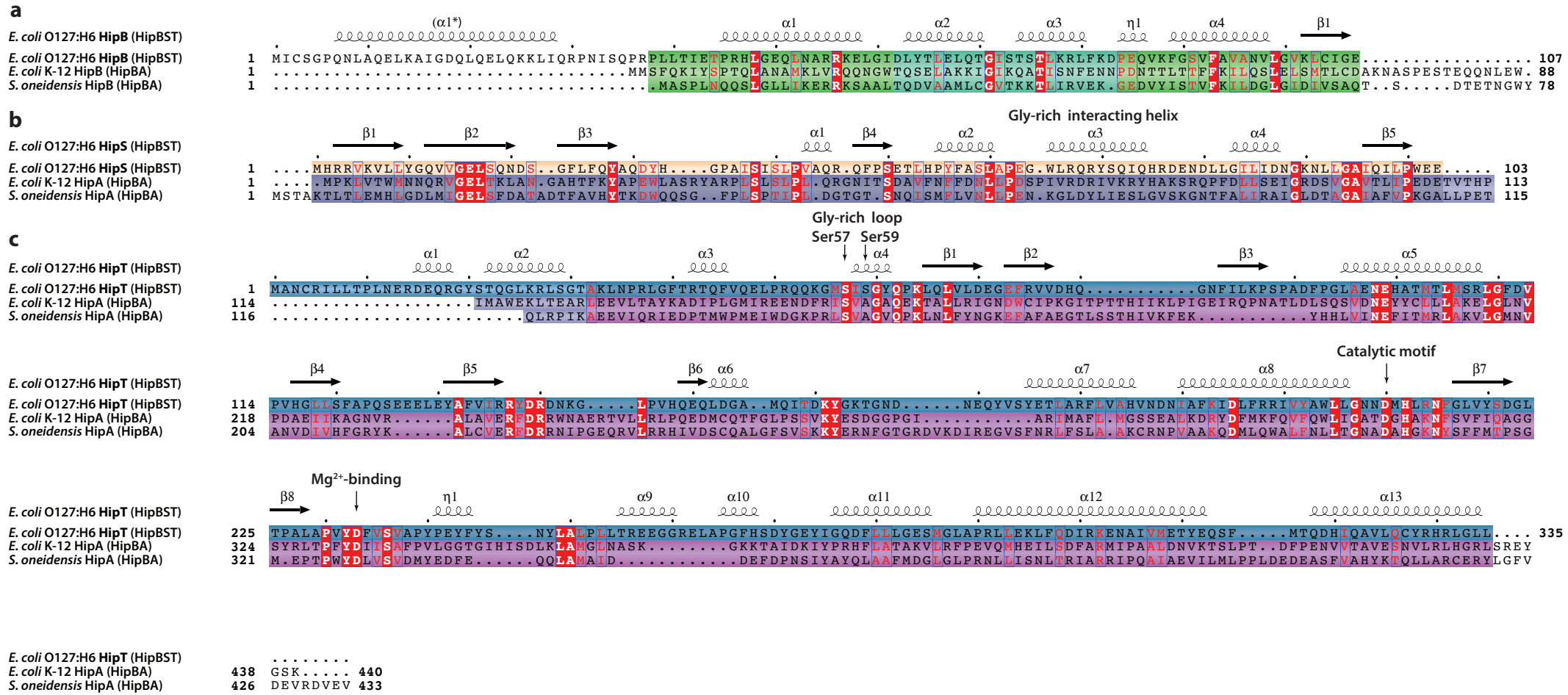
a
E. coli O127:H6 HipB (HipBST)
E. coli O127:H6 HipB (HipBST) 1 MICSGPQNLAQELKAIGDQLQELQKKLIQRPNISQPRPLLTIETPRHLGEQLNARRKELGIDLYTLELQTGISTSTLKRLFKDPEQVKFGSVFAVANVLGVKLCIGE 107
E. coli K-12 HipB (HipBA) 1 MMSFQKIYSPTQLANAMKLVRQQNGWTQSELAKKIGIKQATLSNFENNPDNTTLTTFFKILQSLELSMTLCDAKNASPESTEQQNLEW 88
S. oneidensis HipB (HipBA) 1 MASPLNQQSLGLLIKERRKSAALTQDVAAMLCGVTKKTLIRVEK GEDVYISTVFKILDGLGIDIVSAQT S DTETNGWY 78
b
Gly-rich interacting helix
E. coli O127:H6 HipS (HipBST)
E. coli O127:H6 HipS (HipBST) 1 MHRRVKVLLYGQVVGELSQNDS GFLFQYAQDYH GPAISISLPVAQR QFPSETLHPYFASLAPEG WLRQRYSQIQHRDENDLLGILIDNGKNLLGAIQILPWEE 103
E. coli K-12 HipA (HipBA) 1 MPKLVTWMNNQRVGELTKLAN GAHTFKYAPEWLASRYARPLSLSLPL QRGNITSDAVFNFFDNLLPDSPIVRDRIVKRYHAKSRQPFDLLSEIGRDSVGAVTLIPEDETVTHP 113
S. oneidensis HipA (HipBA) 1 MSTAKTLTLEMHLGDLMIGELSFDATADTFAVHYTKDWQQSG FPLSPTIPL DGTGT SNQISMFLVNLLPEN KGLDYLIESLGVSKGNTFALIRAIGLDTAGAIAFVPKGALLPET 115
c
Gly-rich loop
Ser57 Ser59
E. coli O127:H6 HipT (HipBST)
E. coli O127:H6 HipT (HipBST) 1 MANCRILLTPLNERDEQRGYSTQGLKRLSGTAKLNPRLGFTRTQFVQELPRQQKGMSISGYQPKLQLVLDEGEFRVVDHQ GNFILKPSPADFPGLAENEHATMTLMSRLGFDV
E. coli K-12 HipA (HipBA) 114 IMAWEKLTEARLEEVLTAYKADIPLGMIREENDFRISVAGAQEKTALLRIGNDWCIPKGITPTTHIIKLPIGEIRQPNATLDLSQSVDNEYYCLLLAKELGLNV
S. oneidensis HipA (HipBA) 116 QLRPIKAEEVIQRIEDPTMWPMEIWDGKPRLSVAGVQPKLNLFYNGKEFAFAEGTLSSTHIVKFEK YHHLVINEFITMRLAKVLGMNV
Catalytic motif
E. coli O127:H6 HipT (HipBST)
E. coli O127:H6 HipT (HipBST) 114 PVHGLLSFAPQSEEELEYAFVIRRYDRDNKG LPVHQEQLDGA MQITDKYGKTGND NEQYVSYETLARFLVAHVNDNIAFKIDLFRRIVYAWLLGNNDMHLRNFGLVYSDGL
E. coli K-12 HipA (HipBA) 218 PDAEIIKAGNVR ALAVERFDRRWNAERTVLLRLPQEDMCQTFGLPSSVKYESDGGPGI ARIMAFL MGSSEALKDRYDFMKFQVFQWLIGATDGHAKNFSVFIQAGG
S. oneidensis HipA (HipBA) 204 ANVDIVHFGRYK ALCVERFDRRNIPGEQRVLRRHIVDSCQALGFSVSKKYERNFGTGRDVKDIREGVSFNRLFSLA AKCRNPVAAKQDMLQWALFNLLTGNADAHGKNYSFFMTPSG
Mg2+-binding
E. coli O127:H6 HipT (HipBST)
E. coli O127:H6 HipT (HipBST) 225 TPALAPVYDFVSVAPYPEYFYS NYLALPLLTREEGGRELAPGFHSDYGEYIGQDFLLLGESMGLAPRLLEKLFQDIRKENAIVMETYEQSF MTQDHIQAVLQCYRHRLGLL 335
E. coli K-12 HipA (HipBA) 324 SYRLTPFYDIISAFPVLGGTGIHISDLKLAMGLNASK GKKTAIDKIYPRHFLATAKVLRFPEVQMHEILSDFARMIPAALDNVKTSLPT DFPENVVTAVESNVLRLHGRLSREY
S. oneidensis HipA (HipBA) 321 M EPTPWYDLVSVDMYEDFE QQLAMAID DEFDPNSIYAYQLAAFMDGLGLPRNLLISNLTRIARRIPQAIAEVILMLPPLDEDEASFVAHYKTQLLARCERYLGFV
E. coli O127:H6 HipT (HipBST)
E. coli K-12 HipA (HipBA) 438 GSK 440
S. oneidensis HipA (HipBA) 426 DEVRDVEV 433

Figure S2

a

```
                                   β1        β2        β3                      α1   β4
E. coli O127:H6 HipS     1  .........MHRRVKVLLYGQVVGELS.QNDSGFLFQYAHDY....HGPAISISLPVAQRQFPSE
V. bacterium HipS        1  MTSDASNRVRGRWAEIFQRGVPAGVLEEQAGGGWGFRYLEGY....SGPPVSLTMPVAERSFQFE
B. ovatus HipS           1  .........MSRSAKVYIKGIYAGLLTEIDREHYSFCYDTDYYNNPQLPAVSLTMPKTQQEYTSS
N. bacterium HipS        1  ....MNKGDRERRGVVYVRNIKAGILERSRAG.YRFSYLHEYLTRPDTEPLSLTFPLRRESFESE
Prevotella sp. HipS      1  ..........MKTAIVYLYDRVAGRLTEDENG.FTFLYDPDFLASDGAEAVSLTLPLTDKPYHDT
B. bacterium HipS        1  ..........MRKAAIKIENELAGWLTQDELG.YHFVYEKSYAMKPGARPVSLTLPLRDEPYTSK

E. coli K-12 HipA        1  ..........MPKLVTWMNNQRVGELTKLANGAHTFKYAPEWLASRYARPLSLSLPLQRGNITSD

                                α2          α3                α4              β5
E. coli O127:H6 HipS    52  TLHPYFASLAPEGWL.RQRYSQIQHRDENDLLGMLIDNGK.NLLGAIQILPWEE..........
V. bacterium HipS       62  EFPAIFEGLLPEGPQ.LEALLRTHKIDRNDAFRQLVTVGA.DVVGSLTVAEGADDHQKEKE....
B. ovatus HipS          57  YLFPVFFNMTSEGDN.RIIQARNLHIDEEDDFGILLATAHTDTIGAITVKRI............
N. bacterium HipS       61  KMFPYFLGLIPEGWLL.DLTMRTLKIDPENVFELLLCCCK.DCVGTTSIYPEGEEVK........
Prevotella sp. HipS     55  VLFPFFDGLIPEGWLL.DIAEKSWKINQRDRMSLLLACCK.DCIGAVSVVPEQDDKEEEN.....
B. bacterium HipS       55  VLFPFFDGLIPEGWLL.DIAERNWKLNPRDRMGLLLVCCK.DCIGNVSVEAINEENLP.......

E. coli K-12 HipA       56  AVFNFFDNLLPDSPIVRDRIVKRYHAKSRQPFDLLSEIGR.DSVGAVTLIPEDETVTHPIMAWEK
```

b

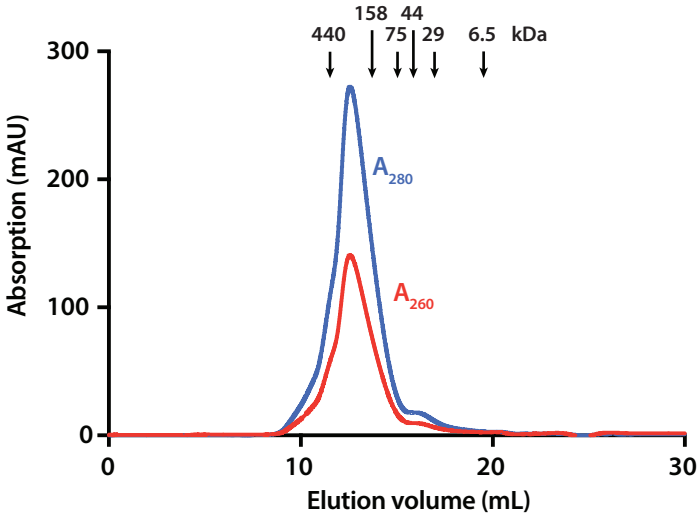

c

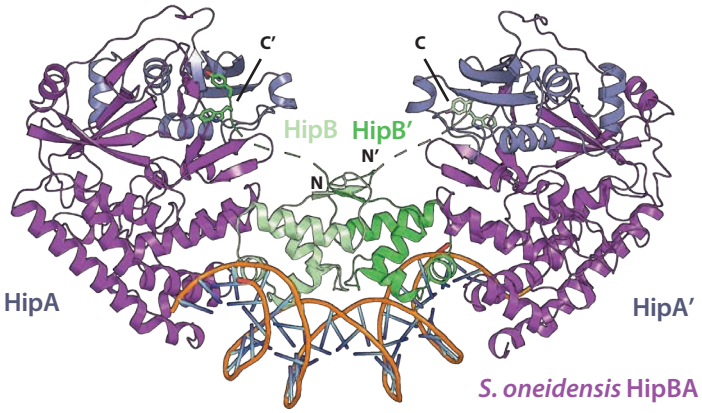

Figure S3

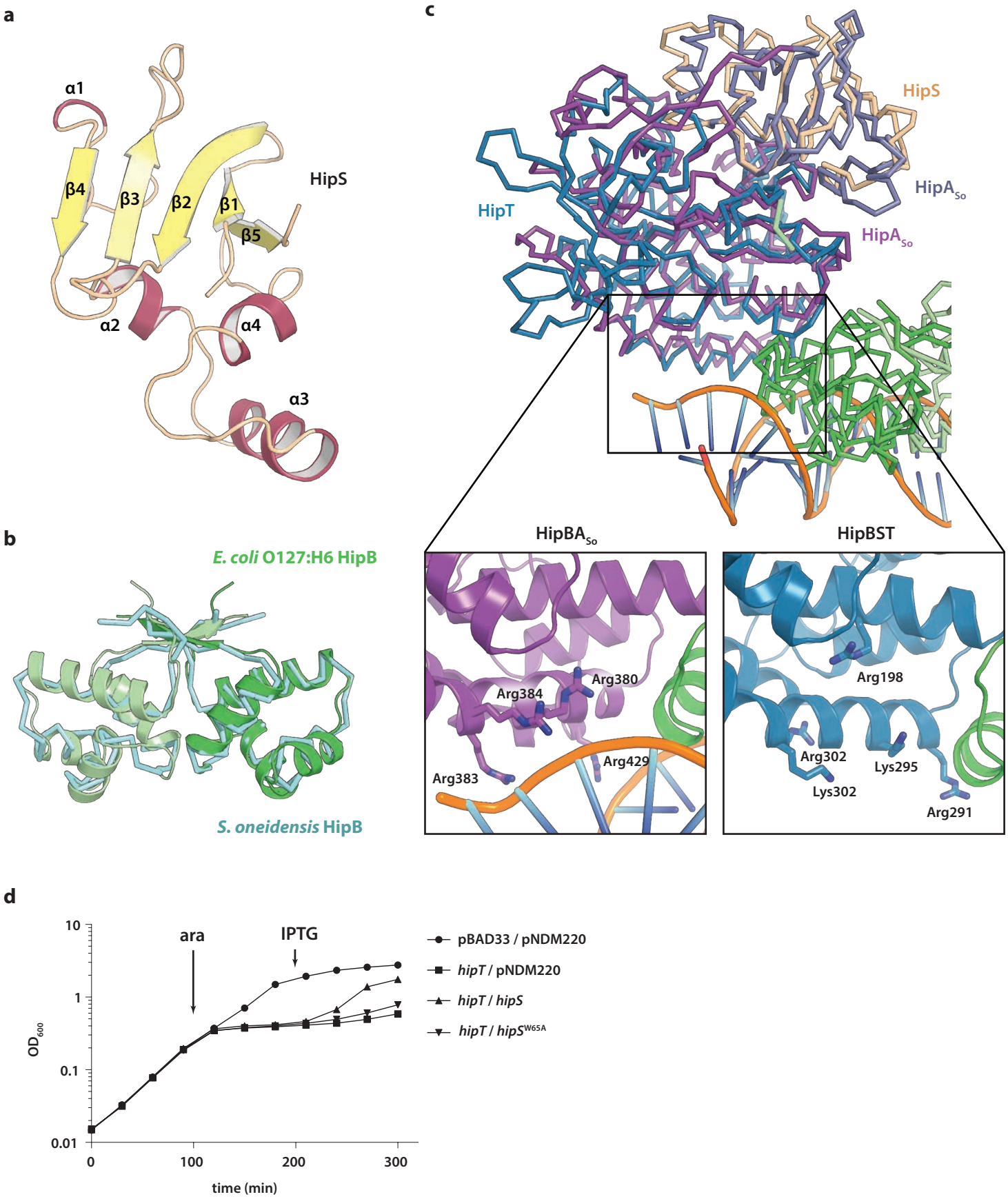
a
α1
β4
β3
β2
β1
β5
HipS
α2
α4
α3
b
E. coli O127:H6 HipB
S. oneidensis HipB
c
HipS
HipA$_{So}$
HipT
HipA$_{So}$
HipBA$_{So}$
HipBST
Arg384
Arg380
Arg429
Arg383
Arg198
Arg302
Lys295
Lys302
Arg291
d
ara
IPTG
10
1
0.1
0.01
OD$_{600}$
0
100
200
300
time (min)
pBAD33 / pNDM220
hipT / pNDM220
hipT / hipS
hipT / hipS^{W65A}

Figure S4

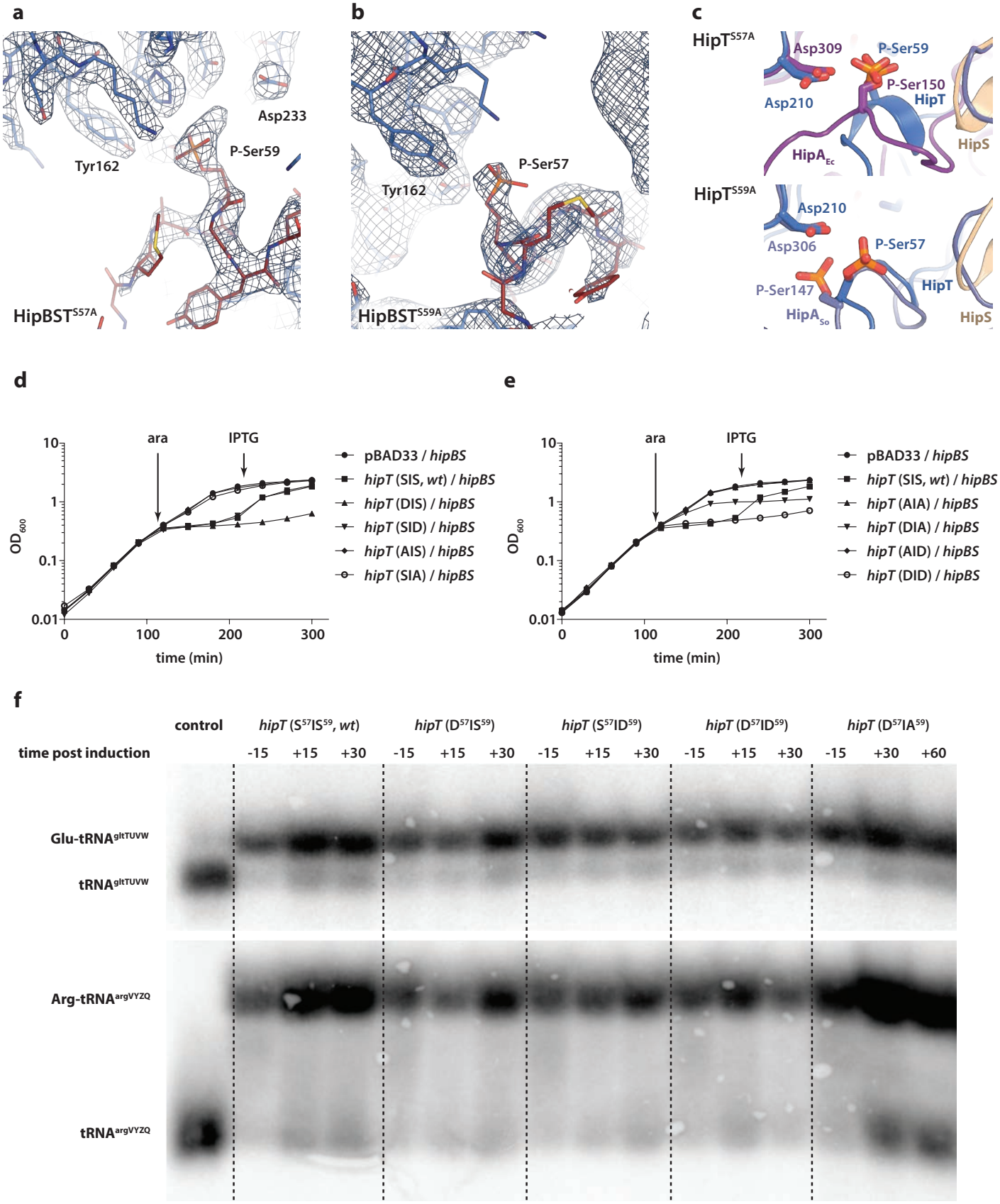
a
Asp233
P-Ser59
Tyr162
HipBST^{S57A}
b
P-Ser57
Tyr162
HipBST^{S59A}
c
HipT^{S57A}
Asp309
P-Ser59
P-Ser150
HipT
Asp210
HipA$_{Ec}$
HipS
HipT^{S59A}
Asp210
Asp306
P-Ser57
P-Ser147
HipT
HipA$_{So}$
HipS
d
ara
IPTG
OD$_{600}$
time (min)
pBAD33 / hipBS
hipT (SIS, wt) / hipBS
hipT (DIS) / hipBS
hipT (SID) / hipBS
hipT (AIS) / hipBS
hipT (SIA) / hipBS
e
ara
IPTG
OD$_{600}$
time (min)
pBAD33 / hipBS
hipT (SIS, wt) / hipBS
hipT (AIA) / hipBS
hipT (DIA) / hipBS
hipT (AID) / hipBS
hipT (DID) / hipBS
f
control
hipT (S^{57}IS^{59}, wt)
hipT (D^{57}IS^{59})
hipT (S^{57}ID^{59})
hipT (D^{57}ID^{59})
hipT (D^{57}IA^{59})
time post induction
-15 +15 +30 -15 +15 +30 -15 +15 +30 -15 +15 +30 -15 +30 +60
Glu-tRNA^{gltTUVW}
tRNA^{gltTUVW}
Arg-tRNA^{argVYZQ}
tRNA^{argVYZQ}

Figure S5

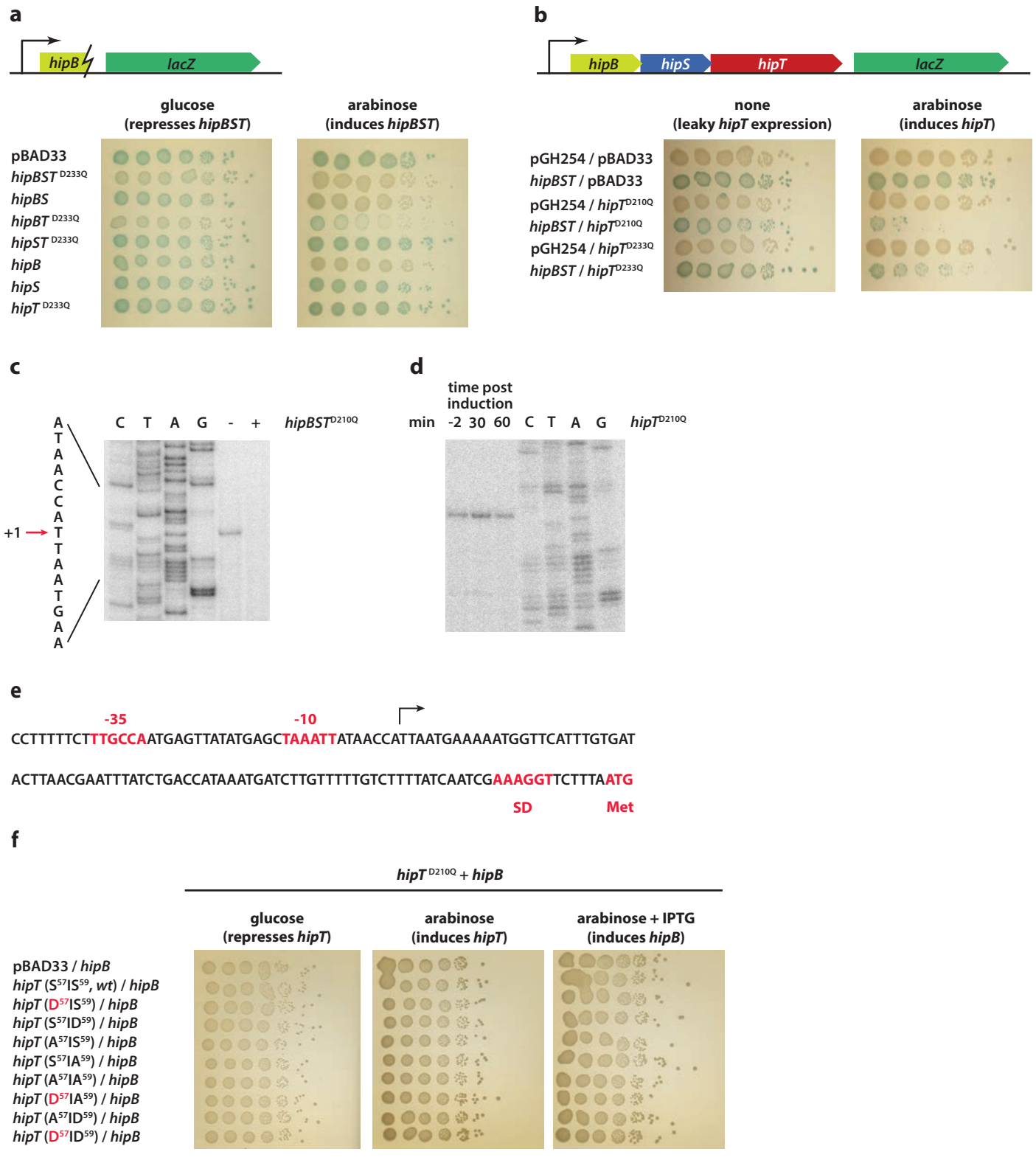
a
hipB
lacZ
glucose
(represses hipBST)
arabinose
(induces hipBST)
pBAD33
hipBST D233Q
hipBS
hipBT D233Q
hipST D233Q
hipB
hipS
hipT D233Q
b
hipB
hipS
hipT
lacZ
none
(leaky hipT expression)
arabinose
(induces hipT)
pGH254 / pBAD33
hipBST / pBAD33
pGH254 / hipT D210Q
hipBST / hipT D210Q
pGH254 / hipT D233Q
hipBST / hipT D233Q
c
A T A A C C A T T A A T G A A
+1
C T A G - +
hipBST D210Q
d
time post
induction
min -2 30 60 C T A G
hipT D210Q
e
-35
-10
CCTTTTTCTTTGCCAATGAGTTATATGAGCTAAATTATAACCATTAATGAAAAATGGTTCATTTGTGAT
ACTTAACGAATTTATCTGACCATAAATGATCTTGTTTTTGTCTTTTATCAATCGAAAGGTTCTTTAATG
SD
Met
f
hipT D210Q + hipB
glucose
(represses hipT)
arabinose
(induces hipT)
arabinose + IPTG
(induces hipB)
pBAD33 / hipB
hipT (S57IS59, wt) / hipB
hipT (D57IS59) / hipB
hipT (S57ID59) / hipB
hipT (A57IS59) / hipB
hipT (S57IA59) / hipB
hipT (A57IA59) / hipB
hipT (D57IA59) / hipB
hipT (A57ID59) / hipB
hipT (D57ID59) / hipB

Figure S6

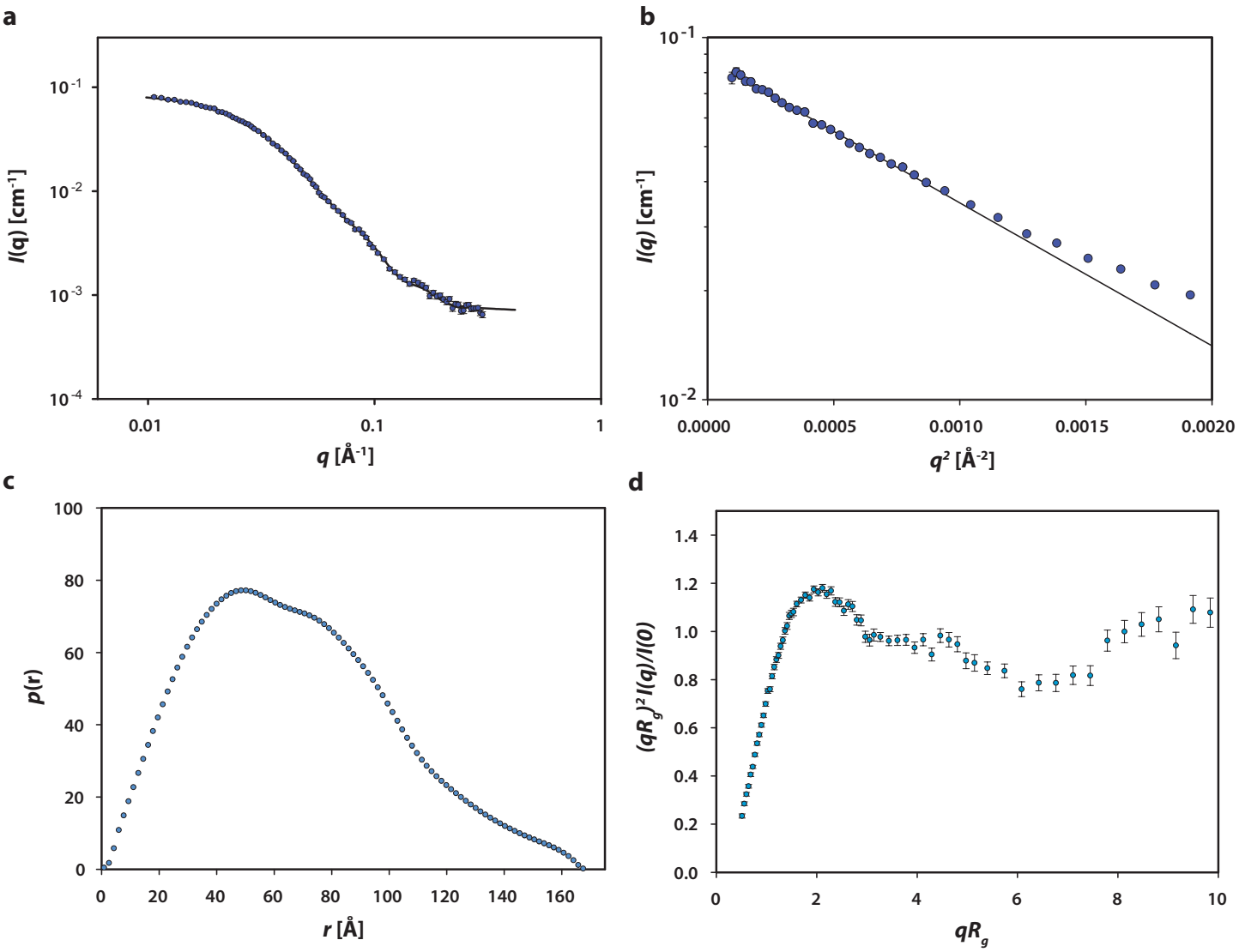

Figure S7

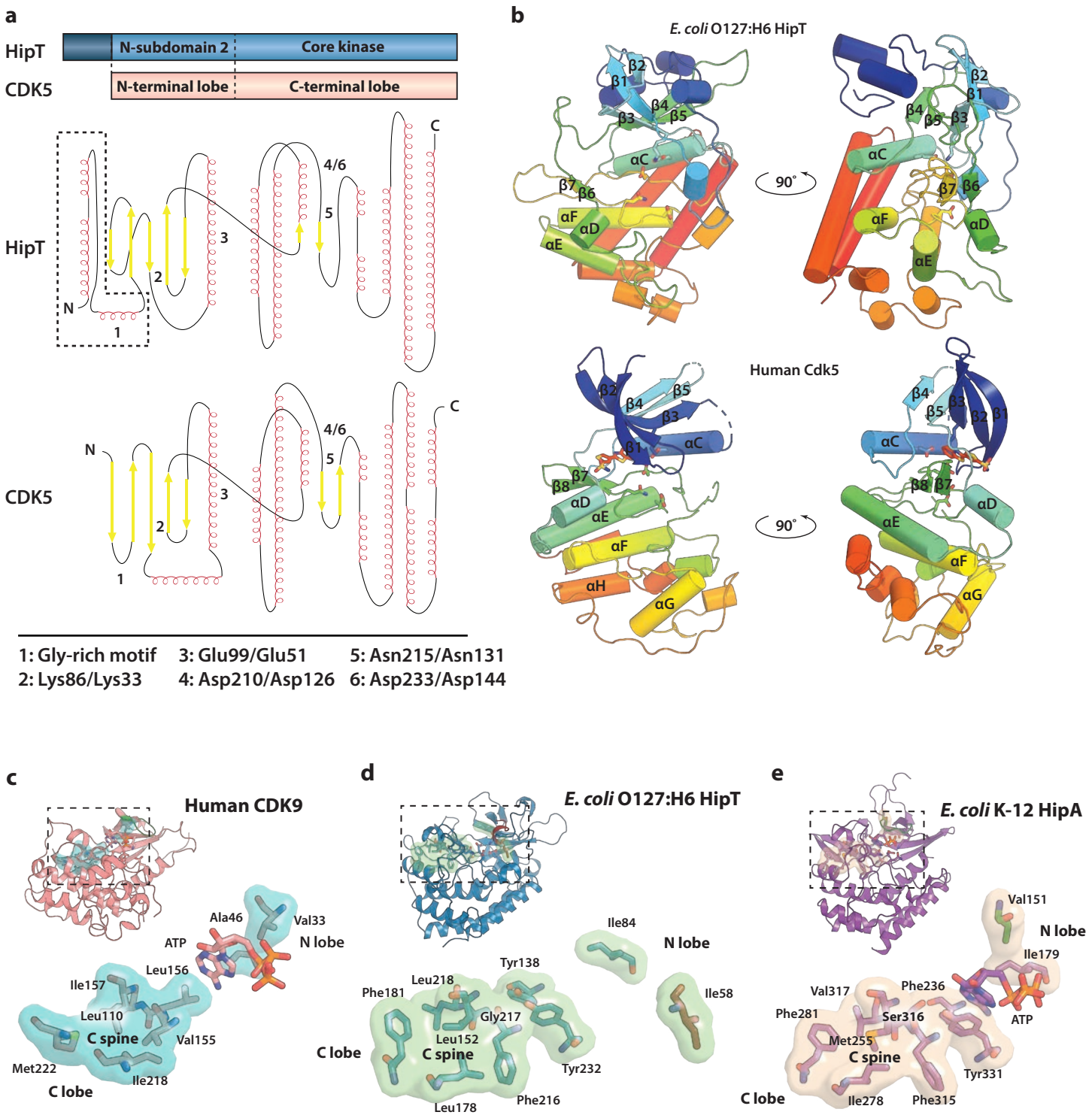
a
HipT
N-subdomain 2
Core kinase
CDK5
N-terminal lobe
C-terminal lobe
HipT
CDK5
N
C
1
2
3
4/6
5
1: Gly-rich motif
2: Lys86/Lys33
3: Glu99/Glu51
4: Asp210/Asp126
5: Asn215/Asn131
6: Asp233/Asp144
b
E. coli O127:H6 HipT
Human Cdk5
90°
c
Human CDK9
ATP
Ala46
Val33
N lobe
Leu156
Ile157
Leu110
C spine
Val155
Met222
Ile218
C lobe
d
E. coli O127:H6 HipT
Ile84
N lobe
Tyr138
Leu218
Phe181
Ile58
Gly217
Leu152
C spine
C lobe
Tyr232
Phe216
Leu178
e
E. coli K-12 HipA
Val151
N lobe
Ile179
Val317
Phe236
Phe281
Ser316
ATP
Met255
C spine
Tyr331
C lobe
Ile278
Phe315